

IL-MCAM: An Interactive Learning and Multi-channel Attention Mechanism-based Weakly Supervised Colorectal Histopathology Image Classification Approach

Haoyuan Chen^a, Chen Li^{a,*}, Xiaoyan Li^{b,*}, Md Mamunur Rahaman^a, Weiming Hu^a, Yixin Li^a, Wanli Liu^a, Changhao Sun^{a,c}, Hongzan Sun^d, Xinyu Huang^e, Marcin Grzegorzec^e

^a*Microscopic Image and Medical Image Analysis Group, College of Medicine and Biological Information Engineering, Northeastern University, China*

^b*Department of Pathology, Cancer Hospital of China Medical University, Liaoning Cancer Hospital and Institute, China*

^c*Shenyang Institute of Automation, Chinese Academy of Sciences, China*

^d*Department of Radiology, Shengjing Hospital of China Medical University, China*

^e*Institute of Medical Informatics, University of Luebeck, Germany*

Abstract

In recent years, colorectal cancer has become one of the most significant diseases that endanger human health. Deep learning methods are increasingly important for the classification of colorectal histopathology images. However, existing approaches focus more on end-to-end automatic classification using computers rather than human-computer interaction. In this paper, we propose an IL-MCAM framework. It is based on attention mechanisms and interactive learning. The proposed IL-MCAM framework includes two stages: automatic learning (AL) and interactivity learning (IL). In the AL stage, a multi-channel attention mechanism model containing three different attention mechanism channels and convolutional neural networks is used to extract multi-channel features for classification. In the IL stage, the proposed IL-MCAM framework continuously adds misclassified images to the training set in an interactive approach, which improves the classification ability of the MCAM model. We carried out a comparison experiment on our dataset and an extended experiment on the HE-NCT-CRC-100K dataset to verify the performance of the proposed IL-MCAM framework, achieving classification accuracies of 98.98% and 99.77%, respectively. In addition, we conducted an ablation experiment and an interchangeability experiment to verify the ability and interchangeability of the three channels. The experimental results show that the proposed IL-MCAM framework has excellent performance in the colorectal histopathological image classification tasks.

Keywords: Colorectal cancer histopathology image, Attention mechanism, Interactivity learning, Image classification

1. Introduction

Cancer is a life-threatening disease caused by the over-proliferation of cells in the human body. Because cancer growth is uncontrollable and irregular, cancer can invade the surrounding tissues and rapidly metastasise to other body parts through the circulatory or lymphatic systems. Colorectal cancer (CRC) is a common type of intestinal cancer. CRC

is initially a polyp, and with time it transforms into cancerous cells. CRC has a high incidence and mortality rate. Among cancers, it has the third highest incidence and second highest mortality rate in the world [1, 2]. In China, the age-standardized incidence of CRC in 2018 is 28.1 per 100,000 and 19.4 per 100,000 for men and women, respectively, and this is increasing annually [3]. Therefore, it is imperative for doctors to diagnose colorectal cancer quickly and accurately.

The traditional approach for diagnosing CRC is for histopathological examination. The pathologist stains the tissue specimen with haematoxylin

*Corresponding author:

**Corresponding author:

Email addresses: lichen201096@hotmail.com (Chen Li), lixiaoyan@cancerhosp-ln-cmu.com (Xiaoyan Li)

and eosin (H&E), and then determines the area of malignancy by observing changes in cell morphology and tissue composition under a microscope [4]. However, the results obtained by pathologists are often time-consuming and highly subjective, which makes histopathological evaluation by pathologists alone inadequate [5]. Therefore, the emergence of rapid and efficient computer-aided diagnosis (CAD) technology is crucial. CAD assists doctors in improving the quality and efficiency of diagnosis in medical images through image processing, pattern recognition and machine learning [6].

Traditional CAD approaches usually use classical machine learning methods, which work as follows: First, the image features, such as shape, colour and texture, are extracted manually. Then the extracted features are classified by a classifier [7]. With the advent of deep learning, the subjective extraction of features in machine learning has been replaced by automatic feature learning in computers using convolutional neural network (CNN) models, thereby dramatically increasing the accuracy and efficiency of CAD [8]. However, CNN models have a disadvantage in that they do not appropriately extract valid information from small-scale datasets. This disadvantage makes it especially important to combine CNN models with an attention mechanism (AM). AM is an approach that assigns the computational resources in favour of the most informative component of the signal [9]. AM approaches mainly represent the automatic selection of attention regions in computer vision tasks. Different AM approaches can be separated into spatial, channel and mixed domains depending on the different priorities of computational resource allocation, leading to different AM approaches having different attention regions within the same task. In medical image datasets, complex components and limited differentiation between different stages make identification of attention regions difficult using a single AM. Consequently, we propose the IL-MCAM framework: a weakly supervised learning approach based on multi-channel attention mechanism (MCAM) and interactive learning (IL) to improve accuracy in colorectal histopathological image classification (CHIC) tasks. The whole process of this approach is shown in Fig. 1.

The training process is separated into two stages: automatic learning (AL) stage and IL stage. The AL stage is performed with the MCAM model, consisting of three channels: spatial information channel (SIC), multi-scale global information channel

(MGIC) and multi-scale spatial information channel (MSIC). The training images are input into the MCAM model to obtain the model parameters of the AL stage using the weighted voting approach after several epochs. In the IL stage, the validation images are input into the previously trained model for classification. Misclassified images are manually labelled with attention regions and then added to the training set for retraining. This process is iterated several times until no new errors are generated in the IL stage. Finally, the model parameters of the final iteration are preserved, and the test images are input to obtain the CHIC task results.

The contributions of this paper are as follows:

- First, the MCAM model can identify the attention regions as accurately as possible in the channel and spatial dimensions by integrating different attention mechanisms, thereby improving the accuracy of the CHIC task in the AL stage.
- Second, the IL approach manually labels attention regions, enabling modification of the errors caused by the MCAM model in the AL stage, which further improves the accuracy of the CHIC task in the IL stage.

This paper is organised as follows: Section 2 provides a review of the status of CHIC tasks in the past few years, Section 3 details the approaches in this paper, Section 4 presents experimental results, Section 5 analyses the reasons based on the experimental results. Finally, Section 6 concludes the paper with a brief conclusion.

2. Related Work

2.1. Classification tasks in Colorectal Histopathology Research

In CHIC tasks, there are several examples of machine learning approaches for classification by manually extracting image features into classifiers. In [10], local binary pattern (LBP) texture features with an integrated contrast measured through a support vector machine (SVM) classifier obtained a 99.5% accuracy in normal-abnormal binary classification of 643 patient-level images. In [11], 60 normal and abnormal images are extracted with mean and variance features and grey-level co-occurrence matrix (GLCM) features. The extracted features are used for classification by the SVM classifier,

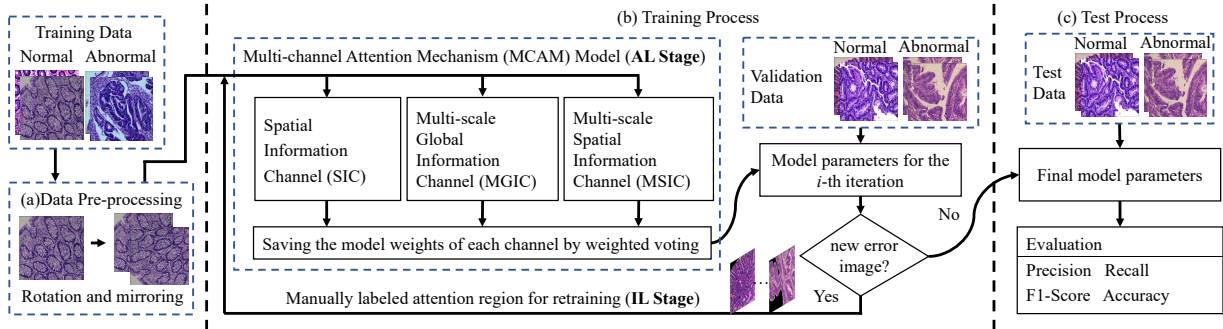


Figure 1: The whole process of IL-MCAM framework.

and an 89.5% F1-score in binary classification is obtained after 3-fold cross-validation. In [12], the experimental process is as follows: The texture features, including LBP, Haraclick features and local intensity order patterns, are dimensionally reduced using principal component analysis, and then different classifiers are used to classify the reduced dimensional features. The experiment achieves 91.3% accuracy for 464 images using the SVM classifier. In [13], the integration features, including three different texture features, Laplacian-of-Gaussian filter, discrete wavelets and GLCM, are used for classification in a linear discriminant analysis classifier. An accuracy of 98.2% is obtained for 480 colorectal histopathology images. In [14], the histogram-low features of 5000 patch-level images using the rbf-SVM classifier obtained 98.6% accuracy in the binary classification problem.

In recent years, with the eminence of deep learning in regular image classification tasks, an increasing amount of research has been conducted on CHIC tasks. In [15], a semi-supervised classification approach based on restricted Boltzmann machines (RBMs) is proposed. This approach uses the features of the sub-regions in the image for learning. A deep belief network of consecutive RBMs is constructed to extract pixels. The activation values of the hidden unit nodes of the RBM are used as the final features. The extracted features are learned using an unsupervised clustering approach. Two datasets containing 3236 and 1644 images is used in multi-classification and obtained accuracies of 96.11% and 78.99%, respectively. In [16], a new adaptive CNN implementation model that performs well even in low-resolution and constrained images is proposed. Using this approach, an accuracy of 94.5% is achieved for 3200 patch-

level images. In [17], a CNN based on a modified VGG model is proposed for CRC classification. An accuracy of 82% is achieved for 10280 images. In [18], a dynamic ensemble learning method is proposed for a multiclass CHIC task. This approach first uses transfer learning to train each model and then a particle swarm optimisation algorithm to select and integrate the models. It obtains an accuracy of 94.52% for 5000 patch-level histopathology images using the ResNet-121 architecture. In [19], a multi-classification accuracy of 95.3% is achieved for 410 patient-level images using a combination of classical CNN and CapsNet models. In [20], an ensemble model based on Xception, DenseNet-121 and InceptionResNet-V2 achieves 92.83%, 96.16% and 99.13% accuracy for CRC-5000, NCT-CRC-HE-100K and the merged datasets, respectively. Similarly, in [21], the ResNet model using fine-tuning achieves 96.77%, 99.76% and 99.98% accuracy for CRC-5000, NCT-CRC-HE-100K and the merged datasets, respectively. In [22], a 92.083% accuracy is obtained by evaluating 108 different combinations of features and classifiers on the CRC-5000 dataset. In [23], an encoder unit of an autoencoder module and a modified DenseNet-121 architecture are used for the purpose approach. This approach, has an accuracy of 97.2% for the Zenodo-100K colorectal histopathology dataset. In [24], the ResNet-50 model is used on private datasets and obtains an overall accuracy higher than 80%.

2.2. Overview of Deep Learning Methods

In computer vision tasks, CNN models are the most used deep learning methods. The continuous improvement of transformer models and multilayer perceptron (MLP) models has made them popular. Especially, deep learning methods are widely used in many biomedical image analysis tasks, such

as COVID-19 identification [25, 26], microorganism image analysis [27, 28, 29], histopathological image analysis [30, 31, 32, 33, 34], cytopathological image analysis [35, 36, 37] and sperm image analysis [38, 39].

The first application of the CNN model was LeNet, proposed by LeCun et al. in 1989 [40]. In 2012, Krizhevsky et al. proposed AlexNet, which that uses the powerful parallel computing ability of the graphics processing unit to process several matrix operations during training [41]. Since then, deep learning methods have formally replaced traditional machine learning methods. The subsequent improvements for the CNN models focus on three aspects: network depth, network width and hybrid network depth and width. The VGG [42], ResNet [43] and DenseNet [44] models increase the network depth by using small convolutional layers, residual mechanisms and dense layers to improve model performance. The Inception-V3 [45] and Xception [46] models enhance the network width by using multi-scale inception blocks and separable convolutional blocks. Some models such as InceptionResNet [47] and ResNeXt [48] enhance the network's depth and width by combining inception blocks and residual mechanisms in the feature extraction layer of the network, thereby improving the classification task performance.

Transformer models were initially proposed by Vaswani et al. in 2017 for natural language processing tasks [49]. In recent years they have moved to computer vision tasks. Transformer models are divided into two main categories, pure transformer models and transformer models combined with CNN [50]. Pure transformer models include ViT [51], DeiT [52], CaiT [53] and T2T-ViT [54] models. These models directly input the image into the transformer encoder after position encoding. Transformer models combining with CNNs are the BoTNet [55], CoaT [56] and LeViT [57] models, which input the feature maps obtained by convolution of the images into the transformer encoder.

The currently implemented MLP models are the improved versions of transformer models. The MLP-mixer [58] model is improved by replacing the self-attention layers of the ViT model with several perceptrons. The gMLP [59] and ResMLP [60] models add a gate mechanism and a residual mechanism to the MLP-mixer model to improve the performance.

3. IL-MCAM framework

The whole process of the IL-MCAM framework is shown in Fig. 2.

Step 1: In Fig. 2-(a), the original images are proportionally divided into training, validation and test sets.

Step 2: In Fig. 2-(b), the training set images are data augmented using the rotation and expansion approach.

Step 3: In Fig. 2-(c.1), the AL stage is implemented by inputting the training set images into the MCAM model for training. The MCAM comprises of three parallel channels, and each channel is composed of CNN models with integrated attention mechanisms, namely SIC, MGIC, and MSIC. The differences between the three different attention mechanism channels and their corresponding CNN models are listed in Table 1. SIC consists of the VGG-16 [42] model-integrated mixed-domain SimAM [61] to extract spatial image information, and each SimAM block is added to the VGG-16 model after each convolutional layer. MGIC consists of the Inception-V3 [62] model integrated channel domain SE [63] to extract image multi-scale global channel information, and each SE block is added to the Inception-V3 model after each inception block. MSIC consists of the Xception [64] model integrated low-cost channel domain ECA [65] to extract image multi-scale local channel information, and each ECA block is added to the Xception model after each flow block. The three trained channels are distributed using the weighted voting approach for each channel component weight.

Step 4: In Fig. 2-(c.2), the IL stage uses a human-machine interaction. The misclassified images in the validation set are labelled with attention regions and then input into the training set for re-training with a transfer learning approach. This process is repeated for several iterations until there are no new misclassified images in the validation set. The model parameters of the last iteration are reserved as the final output.

Step 5: In Fig. 2-(d), the test set images are tested using the last reserved model parameters to obtain the final classification results.

This section is composed as follows: CNNs are explained in Section 3.1, the transfer learning approach is described in Section 3.2, building a MCAM model is detailed in Section 3.3, and interactive learning strategy is explained in Section 3.4.

3.1. Convolutional Neural Network (CNN)

A CNN is a feedforward neural network that includes the computation of the convolution and depth structure. A CNN consists of several layers, including a convolution layer, pooling layer, and fully connected layer. The convolutional layer, which is the core of the CNN extracts image features using a convolution kernel. The pooling layer is used to compress the input feature map and extract the main features. The fully connected layer connects all features and classifies the output features using a classifier. In a CNN, the information extracted by the convolution layers of different networks is separated into two main categories: global and local. Global information refers to the macroscopic representation of an image in its class and is usually extracted by large convolution kernels and positional coding. Local information, also described as spatial information, represents the features of a restricted region of the image in its class and is usually extracted by a small convolution kernel.

The Visual Geometry Group (VGG) proposed the VGG-16 [42] model at the University of Oxford in 2014. Its novelty contribution is raising the

depths of networks from eight to 16, and converting large convolution kernels such as 7×7 and 5×5 into two or three 3×3 small convolution kernels. It is another milestones in deep learning after AlexNet [41] and the baseline for comparing new methods in the field of deep learning. The VGG model has significant advantages. It uses the small convolution kernel to enhance the extraction of spatial information better [66].

The Inception-V3 [62] model is another method that modifies AlexNet [41] and is based on GoogLeNet [67], proposed by Szegedy et al. in 2015. Instead of using the conventional method to increase the number of network layers, the Inception-V3 model uses a novel convolution method to decompose large filter sizes by using parallel convolution and factorised convolution. The entire decomposition module is called the inception structure. Moreover, this model has five different inception structures, each with its own set of components. The Inception-V3 model uses an inception module instead of a large convolution kernel and a global average pooling layer instead of a fully connected layer, to substantially reduce the number of parameters compared with other models. Among

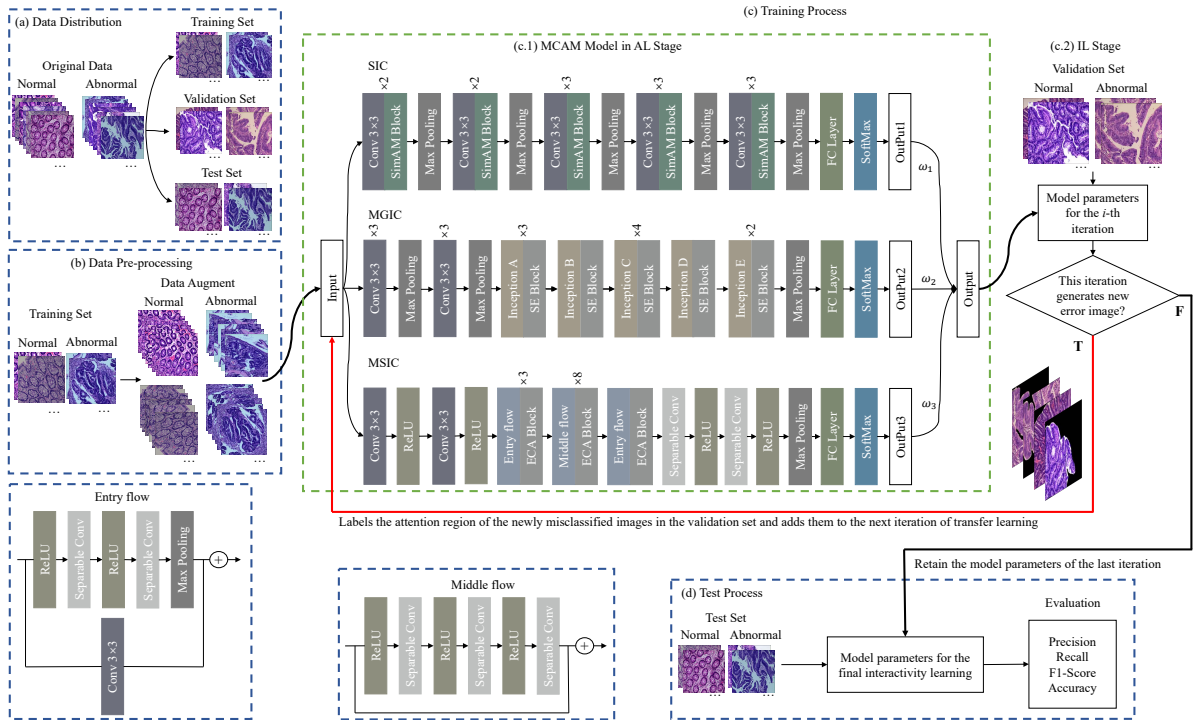


Figure 2: The structure of the proposed IL-MCAM framework.

Table 1: The differences between three different attention mechanism channels and their corresponding CNN models. The bottom row shows classification layers and other rows are feature extraction layers.

VGG-16	SIC	Inception-V3	MGIC	Xception	MSIC
Conv	Conv SimAM Block	Conv	Conv	Conv	Conv
Conv	Conv SimAM Block	Conv	Conv	ReLU	ReLU
Maxpool	Maxpool	Maxpool	Maxpool	Conv	Conv
Conv	Conv SimAM Block	Conv	Conv	ReLU	ReLU
Conv	Conv SimAM Block	Conv	Conv	Entry flow	Entry flow ECA Block
Maxpool	Maxpool	Maxpool	Maxpool	Entry flow	Entry flow ECA Block
Conv	Conv SimAM Block	Inception A	Inception A SE Block	Entry flow	Entry flow ECA Block
Conv	Conv SimAM Block	Inception A	Inception A SE Block	Middle flow	Middle flow ECA Block
Conv	Conv SimAM Block	Inception A	Inception A SE Block	Middle flow	Middle flow ECA Block
Maxpool	Maxpool	Inception B	Inception B SE Block	Middle flow	Middle flow ECA Block
Conv	Conv SimAM Block	Inception C	Inception C SE Block	Middle flow	Middle flow ECA Block
Conv	Conv SimAM Block	Inception C	Inception C SE Block	Middle flow	Middle flow ECA Block
Conv	Conv SimAM Block	Inception C	Inception C SE Block	Middle flow	Middle flow ECA Block
Maxpool	Maxpool	Inception C	Inception C SE Block	Middle flow	Middle flow ECA Block
Conv	Conv SimAM Block	Inception D	Inception D SE Block	Middle flow	Middle flow ECA Block
Conv	Conv SimAM Block	Inception E	Inception E SE Block	Entry flow	Entry flow ECA Block
Conv	Conv SimAM Block	Inception E	Inception E SE Block	Separable Conv	Separable Conv
				ReLU	ReLU
				Separable Conv	Separable Conv
				ReLU	ReLU
Maxpool	Maxpool	Maxpool	Maxpool	Maxpool	Maxpool
FC Layer	FC Layer	FC Layer	FC Layer	FC Layer	FC Layer
Softmax	Softmax	Softmax	Softmax	Softmax	Softmax

CNN models, Inception-V3 has an exceptional ability to extract global multiscale information owing to its parallel convolution structure and partially large convolution kernels.

The Xception [64] model improves the Inception-V3 [62] model by combining the depth-separable convolution [68] and residual mechanism [43]. Unlike the standard convolution approach, depth-separable convolution is performed separately for each channel in the feature map [68]. The advantage of Xception is its combination of the residual structure and depth-separable convolution. The depth-separable convolution effectively extracts the multi-scale features of the image, and the residual mechanism makes the network model converge easily. In contrast to the Inception-V3 model, the small convolutional kernel in depth-separable con-

volution gives the Xception model a good local multi-scale information extraction ability.

3.2. Transfer Learning (TL)

Training CNN models from scratch requires a large amount of data and high computational power, resulting in a longer training time. Moreover, the small size and vague labels of medical datasets make TL critical for CHIC tasks [69]. TL is a machine learning approach wherein a pre-trained model is reused in another task [70]. The TL process has two steps: the first is selecting an original dataset and pre-training on the original dataset. The second is to fine-tune the pre-trained model using the dataset of the target task.

In this paper, we use the ImageNet dataset as the original dataset to pre-train the model. Because low

workstation computing power makes it challenging to pre-train MCAM models directly using the TL approach, we make changes based on traditional transfer learning. The pre-training parameters of the traditional VGG-16, Inception-V3, and Xception models in the Pytorchvision package are loaded layer by layer according to the same parts of SIC, MGIC and MSIC as in Table 1, which are frozen in training. Only AM layers and fully connected layers are used for fine-tuning, and the weights of each channel are assigned using weighted voting.

3.3. Multi-Channel Attention Mechanisms

AMs are inspired by human biological systems. They tend to focus on specific parts when processing large sets of information [9]. The AM approach has become one of the most imperative concepts in the field of deep learning [71]. However, traditional AMs have several disadvantages. For example, a single AM can identify redundant information, leading to mistakes. To overcome some reduce the disadvantages of AMs, we propose an MCAM model. This model extracts features from multiple perspectives through three channels: SIC, MGIC and MSIC. These three complementary channels improve the precision of identifying attention regions and the accuracy of classification tasks.

SIC: SIC is expectation because its capability of extracting spatial information is excellent. The SimAM attention mechanism has an outstanding ability to distribute weights to the features of spatial dimensions [61]. The structure of the SimAM attention mechanism is illustrated in Fig. 3-(a). In visual neuroscience, the most informative neurons show different firing patterns in the surrounding neurons and keep the activity of the surrounding neurons, a phenomenon known as spatial suppression [72]. The easiest way to find these spatially suppressed neurons is to measure the linear separability between the target and other neurons. In computer vision tasks, the edge features of images often play a crucial role in classification tasks. Furthermore, the edge features of images are the same as those of spatial suppression neurons, which often exhibit incredibly high contrast with the surrounding colours and textures. Therefore, the SimAM attention mechanism works by using an energy function (EF) from neuroscience to assign weights to different spatial locations. The energy function perceives each pixel of the feature map as a neuron and the minimal energy of neurons can

be expressed as following:

$$e_t^* = \frac{4(\sigma^2 + \lambda)}{(t - \mu)^2 + 2\sigma^2 + 2\lambda} \quad (1)$$

where t is target neuron, i is index over spatial dimension, $\mu = \frac{1}{M} \sum_{i=1}^M x_i$ and $\sigma^2 = \frac{1}{M} \sum_{i=1}^M (x_i - \mu)^2$ are mean and variance calculated over all neurons except t in that channel, x_i is other neurons in a same channel, $M = H \times W$ is number of neurons on the channel and λ is a coefficient and is set to $1e - 4$ according to the experiments on the CIFAR datasets [61]. Spatially suppression neurons are less similar to other neurons and exhibit a high linear separability, thus showing a significant deviation in t and u leading to a low e_t^* . Meanwhile, in neuroscience, it is considered that lower energy indicates neurons that are more differentiated from surrounding neurons. Therefore, the weights of each neuron can be calculated from e_t^* . The optimization phase of the whole SimAM attention mechanism is obtained by scaling operator:

$$\tilde{X} = \text{sigmoid}\left(\frac{1}{E}\right) \cdot X \quad (2)$$

where X and \tilde{X} are input feature map and output feature map, E is all e_t^* are grouped in spatial and channel dimensions. Finally, the confidence of each neuron at each place is obtained by sigmoid activation function.

In Section 3.1, it is shown that the VGG-16 model is capable of extracting spatial information [42]. Above all, the SimAM attention mechanism after every convolutional layer in VGG-16 model is designed to extract spatial information in the SIC.

MGIC: In the MGIC, the model is expected to be capable of extracting multi-scale global information. In Section 3.1, it explained that — the Inception-V3 model is the best CNN model that can extract global information [62]. Therefore, the Inception-V3 model is selected to extract features in MGIC. The extraction of multi-scale information in the Inception-V3 model is implemented by concatenating different sized receptive fields, so the multi-scale ability of the Inception-V3 model is represented in the channel domain of each feature map. The SE attention mechanism, which possesses a good distribution of channel weights, is selected to strengthen the importance between the channel features in the MGIC [63]. The structure of the SE attention mechanism is shown in Fig. 3-(b). The SE attention mechanism consists of two phases: squeeze phase and excitation

phase. The SE attention mechanism consists of two phases: squeeze and excitation. The squeeze phase encodes the entire spatial features into a global feature by global average pooling to generate channel-wise statistics. The excitation phase obtains the channel-wise importance using two fully connected layers, a dimensionality-reduction layer and a dimensionality-increasing layer, and the final channel-wise weights are obtained by the sigmoid activation function.

MSIC: This channel is implemented using depth-separable convolution of the Xception [64] model. Depth-separable convolution causes information extracted from each channel of the feature map to be diversified so that multi-scale spatial information can be extracted appropriately. The ECA attention mechanism is used after each flow of the Xception model to strengthen its ability to extract multi-scale information. The ECA attention mechanism uses a low time consumption to assign weights to the importance of the channel information of each feature map [65]. The structure of the ECA attention mechanism is illustrated in Fig. 3-(c). The ECA attention mechanism first uses global average pooling (GAP) to obtain channel-wise information, then uses 1D convolutional that captures cross-channel interaction information with a convolutional kernel of size k , and finally obtains channel-wise weight information using a sigmoid activation function.

Multi-channel fusion approach: This approach is an integrated classifier that relies on the classification decision values of different channels and the weights of each channel to improve the classification performance [36]. In this experiment, the last feature maps of SIC, MGIC and MSIC are used to obtain the classification decision values for each channel using pooling, fully connected and softmax layers. Then, the classification decision values of each channel are weighted and evaluated using grid weighted voting to obtain the classification decision values of the MCAM model. Finally, the category that belongs to the maximum classification decision values of the MCAM model is used as the final classification result. The calculation formula is described as follows:

$$C = \max_{1 < x < n} \sum_{i=1}^3 \omega_i D_i \quad (3)$$

where C is classification category, n is the number of categories, i is the number of channels of the

MCAM model and $D_i = \{d_1, d_2, \dots, d_n\}$ is n classification decision values of i th channel of MCAM model.

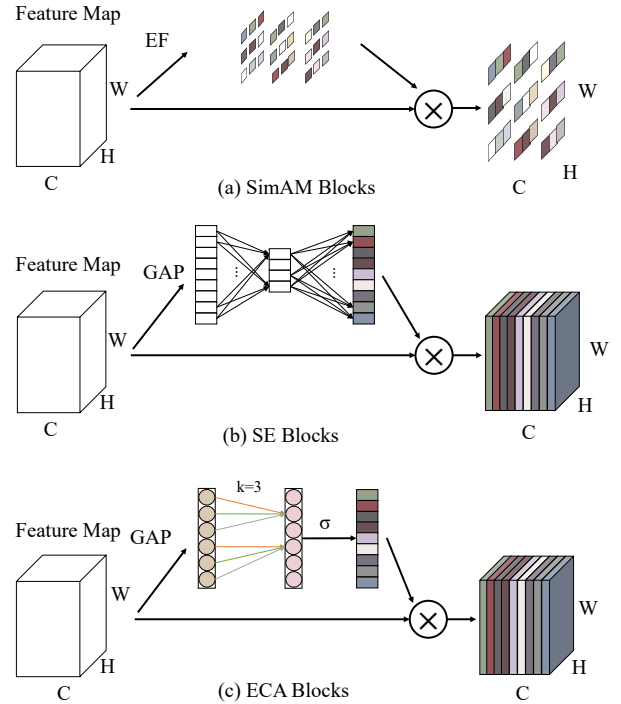


Figure 3: The structure of three different attention mechanism. (a) is SimAM Blocks after each convolution layer in SIC. (b) is SE Blocks after each Inception block in MGIC. (c) is ECA blocks after each flow in MSIC.

3.4. Interactive Learning (IL)

The substance of the proposed IL-MACM framework is limited frequency incremental learning. Incremental learning means that a learning system can continuously learn from new samples and can preserve most of previously acquired knowledge [73]. The implementation of incremental learning is achieved through an IL strategy. The IL-MACM framework process is shown in Fig. 4. First, the misclassified images in the validation set are sent to the pathologist after one training iteration. The attention regions are then discreetly and meticulously labelled by pathologists. Finally, the labelled images are input into the training set for the next training iteration until no new errors appear in the validation set.

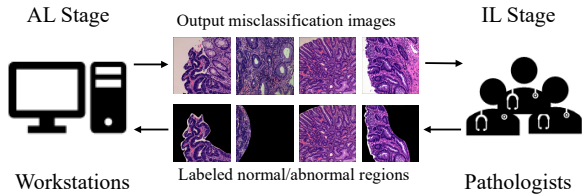


Figure 4: The process of IL-MCAM framework.

4. Experiment Results and Analysis

4.1. Experimental Settings

4.1.1. Dataset

In this study, an haematoxylin and eosin (H&E) stained colorectal cancer (CRC) histopathology dataset (HE-CRC-DS) is used in the experiment to evaluate the classification performance of the proposed IL-MCAM approach. This dataset is collected and labelled by two pathologists from the Cancer Hospital of China Medical University and four biomedical researchers from Northeastern University. Pathologists provide electron microscopy images of histopathological sections of CRC enteroscopic biopsies using an ‘‘Olympus’’ microscope and the ‘‘NewUsbCamera’’ software and also provide image-level annotations of weakly supervised learning processes. Biomedical researchers organise and create datasets. Details of the acquisition of HE-CRC-DS are shown in Fig. 5, and the image-level labels are given as follows: First, when the pathologist finds only the differentiation stage in a $40\times$ image, it is magnified to $200\times$ for preservation, and this differentiation stage is then used as the image-level label. Then, if the physician finds multiple differentiation stages or similar differentiation stages in a $40\times$ image, the most severe stage is magnified to $200\times$ and saved, and the most severe stage is used as the image level label. In summary, the image-level label is the same as the patient-level label in HE-CRC-DS.

HE-CRC-DS includes 4005 images of 2048×1536 pixels in the ‘‘.png’’ file format. The overall magnification of all images in the HE-CRC-DS is $200\times$. Most pathologists classify CRC into five categories: normal, polyp, low grade, high grade, and cancer. Due to the unbalanced data distribution in the initial dataset, this experiment classified the normal category including normal, polyp and low grade with 2031 images and the abnormal category including high grade and cancer with 1974 images.

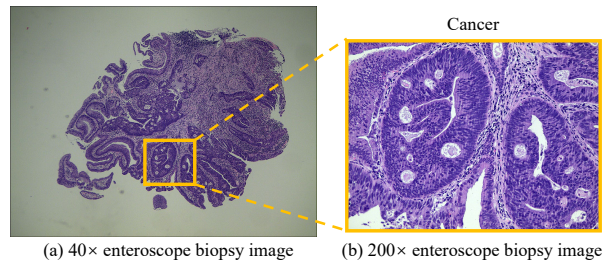


Figure 5: Details of the acquisition of HE-CRC-DS. (a) is a $40\times$ image obtained by enteroscopy biopsy. (b) is a $200\times$ image containing in HE-CRC-DS. Pathologists first assess the most severely differentiation stage in the $40\times$ images. Then the dataset images are obtained by adjusting the magnification to $200\times$ and giving image-level labels according to the most severe differentiation stage.

Examples of the HE-CRC-DS are shown in Fig. 6. The normal category is shown in Fig. 6-(a). All of them have intact oval glands with neatly arranged nuclei. The abnormal category is shown in Fig. 6-(b). The boundaries of the glandular structures are not clear and the nuclei are drastically enlarged.

4.1.2. Data Settings

All the images in the HE-CRC-DS, including the normal and abnormal categories, are randomly partitioned into training data and test data at a ratio of 1:1. In the training data, the training and validation sets are randomly assigned three times at a ratio of 1:1 and used to perform three randomised experiments. All of these are resized to 224×224 pixels using bilinear interpolation. Because the small size of the medical image dataset leads to a large amount of error information in training, the training set is enlarged to six times by rotating it 90° , 180° , and 270° and horizontal and vertical mirroring. The biomedical researcher uses the ‘‘MATLAB R2020a’’ software to perform resizing, rotation, and mirroring operations in the pre-processing stage. The pathologist uses the ‘‘Photoshop’’ software to label the attention areas in the IL stage. The normal and abnormal categories of the epithelial tissues are labelled to minimise the impact of mesenchymal misclassification. The data settings are listed in Table 2.

4.1.3. Hyper-parameter Setting

The IL-MCAM framework consists of two stages. In the AL stage, MCAM model uses 100 epochs and 16 batch sizes trained by the HE-CRC-DS. In the AL and IL stages, the model parameters preserved in each iteration are those with the highest

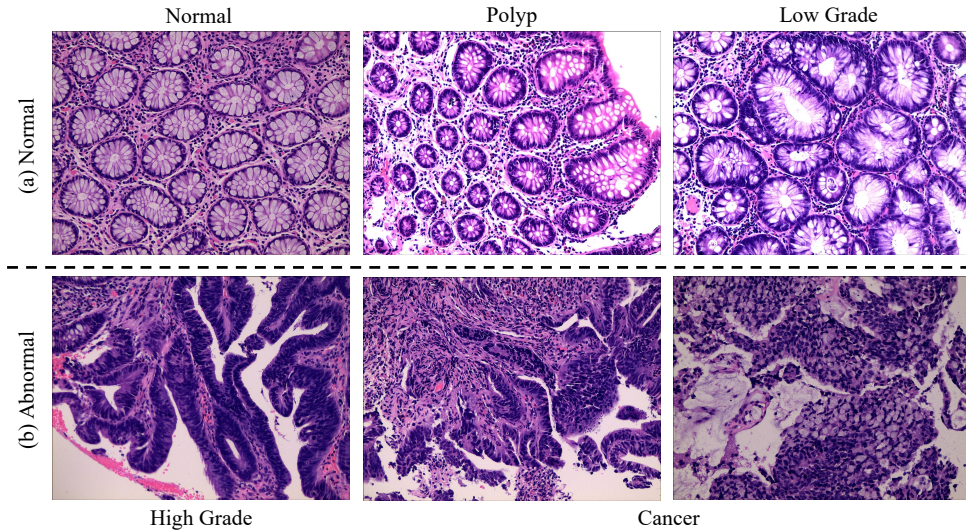


Figure 6: Some examples in the HE-CRC-DS.

Table 2: Data setting of HE-CRC-DS for training, validation and test sets.

Image Type	Training	Validation	Test
Normal	3048	508	1015
Abnormal	2964	493	987
Sum	6012	1001	2002

validation set accuracy in this iteration. It uses a modified transfer learning approach in Section 3.2 for the CHIC task. In the IL stage, one iteration is set to 50 epochs, and only the last fully connected layer is trained using a fine-tuning approach. The AdamW optimiser [74] is used for optimization, and its parameters are set to $2e-3$ learning rate, $1e-8$ eps, $[0.9, 0.999]$ betas and $1e-2$ weight decay.

4.1.4. Evaluation Criteria

To overcome the bias between different algorithms, it is crucial to choose the appropriate evaluation criteria. Specificity (Spec.), sensitivity (Sens.), F1-score (F1) and average accuracy (Avg.Acc.) are the most standard metrics for evaluating classification performance. True positive (TP), true negative (TN), false positive (FP) and false negative (FN) are used to define these criteria in Table 3. Spec. represents to the ratio of all negative samples predicted to be correct to all actual negative samples. Sens. represents the ratio of correctly classified positive samples to all actual positive samples. F1 is a comprehensive considera-

tion of precision and recall, and it is a critical evaluation criterion for evaluating a model. Avg.Acc is the most typical and fundamental evaluation criterion.

Table 3: Criteria and corresponding definitions for image classification evaluation.

Criteria	Definition	Criteria	Definition
Spec.	$\frac{TN}{TN+FP}$	Sens.	$\frac{TP}{TP+FN}$
F1	$\frac{2 \times TP}{2 \times TP + FP + FN}$	Avg.Acc.	$\frac{TP+TN}{TP+TN+FP+FN}$

4.2. Classification Evaluation

4.2.1. Experimental Results

To analyse the experimental results, we show the confusion matrix obtained from three randomised experiments of the proposed MCAM model and IL-MCAM framework in Fig. 7. Three randomised experiments and the average evaluation results of the proposed MCAM model and IL-MCAM framework are shown in Table 4.

In the 1st experiment, the MCAM model is used in the validation and test sets for classification, and the confusion matrix is shown in Figs. 7-(a) and (g). For the validation set, five abnormal category images are misclassified as normal, and five normal category images are misclassified as abnormal. For the test set, 12 abnormal category images are misclassified as normal, and 23 normal category images

are misclassified as abnormal. Additionally, the IL-MCAM framework is also used in the validation and test sets for classification, and the confusion matrix is shown in Figs. 7-(d) and (j). For the validation set, one abnormal category image is misclassified as normal, and three normal category images are misclassified as abnormal. For the test set, eight abnormal category images are misclassified as normal, and 14 normal category images are misclassified as abnormal. In summary, compared with the MCAM model, the IL-MCAM framework identifies two more correct abnormal images and four more normal images in the validation set and identifies nine more correct abnormal images and four more normal images in the test set.

In the 2nd experiment, the MCAM model is used in the validation and test sets for classification, and the confusion matrix is shown in Figs. 7-(b) and (h). For the validation set, nine abnormal category images are misclassified as normal, and four normal category images are misclassified as abnormal. For the test set, 16 abnormal category images are misclassified as normal, and 14 normal category images are misclassified as abnormal. Additionally, the IL-MCAM framework is also used in the validation and test sets for classification. The confusion matrix is shown in Figs. 7-(e) and (k), and the results are the same as those for the MCAM model. These results suggest that the addition of the IL stage did not occur in this randomised experiment.

In the 3rd experiment, the MCAM model is used in the validation and test sets for classification, and the confusion matrix is shown in Figs. 7-(c) and (i). For the validation set, five abnormal category images are misclassified as normal, and six normal category images are misclassified as abnormal. For the test set, 18 abnormal category images are misclassified as normal, and 14 normal category images are misclassified as abnormal. Additionally, the IL-MCAM framework is also used in the validation and test sets for classification, and the confusion matrix is shown in Figs. 7-(d) and (j). For the validation set, no abnormal category images are misclassified as normal, and six normal category images are misclassified as abnormal. For the test set, five abnormal category images are misclassified as normal, and 12 normal category images are misclassified as abnormal. In summary, compared with the MCAM model, the IL-MCAM framework identifies five more correct abnormal images and no more normal images in the validation set and 13 more correct abnormal images and two more normal images

in the test set.

The following results are obtained from Table 4. First, it can be observed that the accuracy of classification results of the first and third randomised experiments using the IL-MCAM framework is higher than that of accuracy using MCAM model, except for the second randomized experiment. In the three randomised experiments, the MCAM model achieves 99.02%, 98.72% and 98.85% on average in the abnormal category of the validation set and 98.32%, 98.45% and 98.37% on average in the abnormal category of the test set for Spec., Sens. and F1, respectively. Based on the MCAM model, using the IL-MCAM framework improve the Spec., Sens., and F1 by 0.13%, 0.60% and 0.37% on average for the abnormal category of the validation set and 0.59%, 0.35% and 0.47% for the abnormal category of the test set, respectively. The Avg.Acc. of the three randomised experiments improves by 0.36% and 0.47% in the validation and test sets, respectively. It is observed that using IL-MCAM framework can improve the classification effect of the MCAM model. Furthermore, in the three randomised experiments, regardless of whether the MCAM model or the IL-MCAM framework is used for classification, the deviations between the accuracies of the validation and test sets are not more than 1.00%. This indicates that the IL-MCAM framework has good extensibility and robustness. Finally, the standard deviations of the three randomized experiments obtained using the MCAM model are 0.12% and 0.10% for the validation and test sets, respectively. The standard deviations of the three randomised experiments using the IL-MCAM framework are 0.39% and 0.27% for the validation and test sets, respectively. The slight fluctuation of the standard deviation indicates that the MCAM model and IL-MCAM framework have good stability.

4.2.2. Contrast Experiment of CHIC

There are three contrast experiments as follows: The first compares the proposed IL-MCAM framework with other traditional deep learning models, the second compares the proposed IL-MCAM framework with models that do not use TL, and the third compares the proposed IL-MCAM framework with models that do not use AM.

Comparison with other deep learning models: To validate the excellent performance of the MCAM model and IL-MCAM framework in the CHIC task, we compare 18 different basic

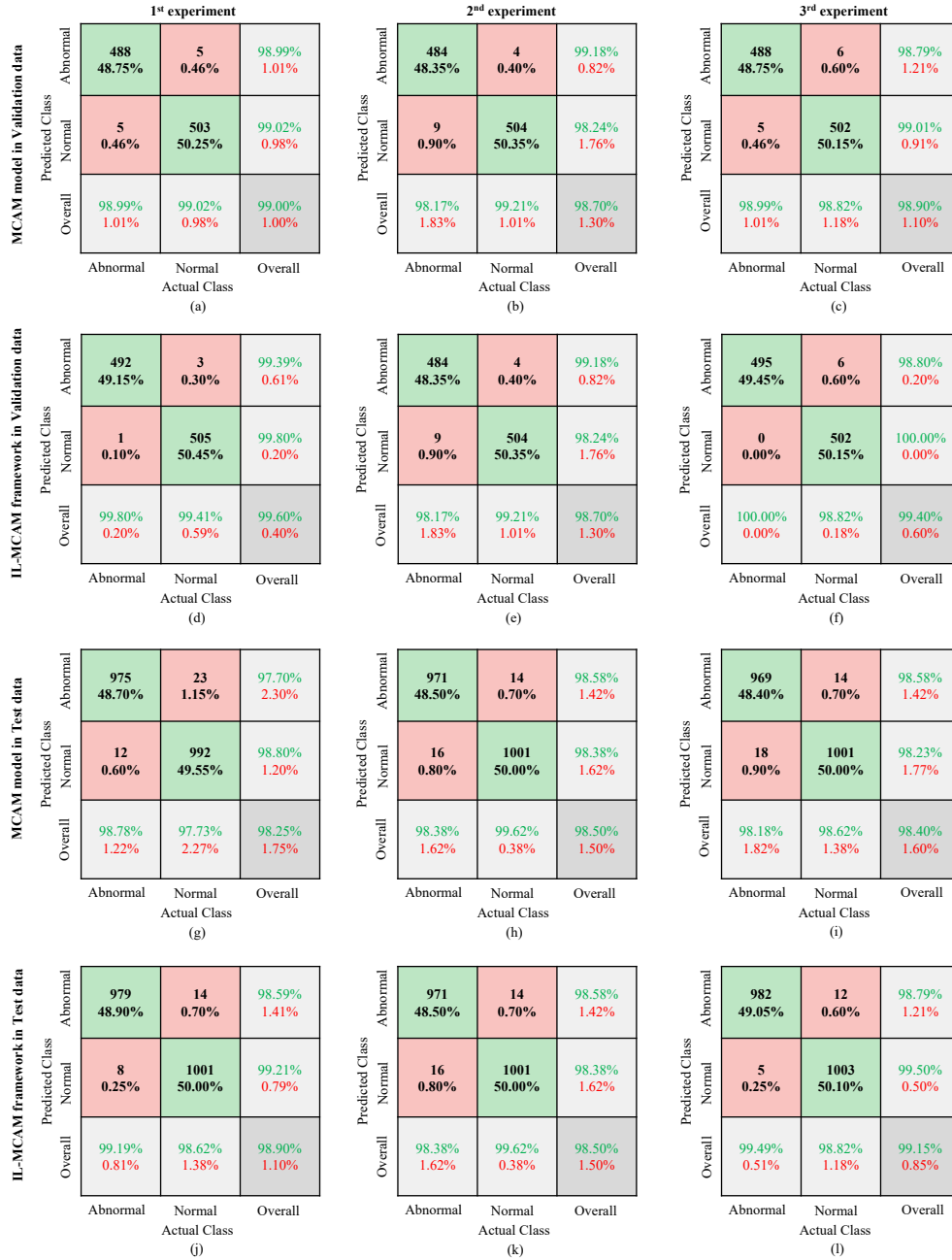


Figure 7: Confusion matrix for three randomised experiments in the CHIC task. 1st to 4th rows are used to represent the results of using MCAM model in validation set, IL-MCAM framework in validation set, MCAM model in test set and IL-MCAM framework in test set, respectively. Each column represents each randomized experiment.

Table 4: Performance analysis of the proposed MCAM model and IL-MCAM framework on validation and test sets among three randomised experiments. ([In %].)

Test Name	Model /Framework	Category	Validation Set				Test Set			
			Spec.	Sens.	F1	Avg.Acc	Spec.	Sens.	F1	Avg.Acc
1 st Experiment	MCAM	Abnormal	99.02	98.99	98.99	99.00	97.73	98.78	98.24	98.25
		Normal	98.99	99.02	99.02		98.78	97.73	98.27	
	IL-MCAM	Abnormal	99.41	99.80	99.60	99.60	98.62	99.19	98.89	98.90
		Normal	99.80	99.41	99.60		99.19	98.62	98.91	
2 nd Experiment	MCAM	Abnormal	99.21	98.17	98.67	98.70	98.62	98.38	98.48	98.50
		Normal	98.17	99.21	98.73		98.38	98.62	98.52	
	IL-MCAM	Abnormal	99.21	98.17	98.67	98.70	98.62	98.38	98.48	98.50
		Normal	98.17	99.21	98.73		98.38	98.62	98.52	
3 rd Experiment	MCAM	Abnormal	98.82	98.99	98.89	98.90	98.62	98.18	98.38	98.40
		Normal	98.99	98.82	98.92		98.18	98.62	98.43	
	IL-MCAM	Abnormal	98.82	100.00	99.39	99.40	99.49	98.82	99.14	99.15
		Normal	100.00	98.82	99.41		98.82	99.49	99.16	
Average	MCAM	Abnormal	99.02	98.72	98.85	98.87 ± 0.12	98.32	98.45	98.37	98.38 ± 0.10
		Normal	98.72	99.02	98.89		98.45	98.32	98.41	
	IL-MCAM	Abnormal	99.15	99.32	99.22	99.23 ± 0.39	98.91	98.80	98.84	98.85 ± 0.27
		Normal	99.32	99.15	99.25		98.80	98.91	98.86	

deep learning models, including CNN models, vision transformer (VT) models and MLP models, which are AlexNet [41], VGG-16 [42], Inception-V3 [45], ResNet-50 [43], Xception [46], ResNeXt-50 [48], InceptionResNet-V1 [47], DenseNet-121 [44], ViT [51], DeiT [52], BoTNet-50 [55], CoaT [56], CaiT [53], T2T-ViT [54], LeViT [57], MLP-Mixer [58], gMLP [59] and ResMLP [60].

The results of the contrast experiment between the IL-MCAM framework and other deep learning models are shown in Table 5. The evaluation criteria are obtained by averaging the results of three the randomised experiments. The following results are obtained and are listed in Table 5 by analysing the performance of traditional deep learning models on the test set. First, Inception-V3, VGG-16 and Inception-V3 have the best Spec., Sens., and F1, respectively, in the abnormal category with values of 98.13%, 98.65% and 98.23%, respectively. Meanwhile, VGG-16, Inception-V3, and Inception-V3 have the best Spec., Sens. and F1, respectively, in the normal with values of 98.65%, 98.13% and 98.23%, respectively. Finally, Inception-V3 has the best Avg.Acc. of 98.25%.

Compared with traditional deep learning models, the proposed MCAM model and IL-MCAM framework can improve the performance. Although Sens. obtained by the MCAM model in the abnormal category is 0.20% lower than the optimal Sens. of the traditional deep learning models, it is higher than that of all other deep learning models except

the VGG-16. Meanwhile, Spec. and F1 obtained by the MCAM model in the abnormal category are 0.19% and 0.12%, respectively, which are better than those of traditional deep learning models. Similarly, the MCAM model improves Spec. and F1 compared to traditional deep learning models in the normal category, except for a slight decrease in Sens. Most importantly, the Avg.Acc. of the MCAM model is 0.13% higher than the optimal result of traditional deep models, indicating that the MCAM model improves the classification performance compared with traditional deep learning models.

Compared with the optimal results obtained by traditional deep learning models, Spec., Sens. and F1 obtained by the IL-MCAM framework in the abnormal category improved by 0.78%, 0.15%, and 0.61%, respectively. In addition, Spec., Sens. and F1 obtained by the IL-MCAM framework in the normal category improved by 0.15%, 0.78%, and 0.60%, respectively, compared with traditional deep learning models. Finally, the Avg.Acc. of the IL-MCAM framework is 0.60% higher than that of traditional deep learning models. The above comparison results indicate that the IL-MCAM framework performs better than traditional deep learning models in the CHIC task.

The contrast experiment result between the IL-MCAM framework and traditional deep learning method shows that the proposed MCAM model has improved significant improvement compared to the

traditional deep learning model in the CHIC task. Furthermore, interactive learning of the IL-MCAM framework can further improve the classification performance of the MCAM model.

Comparison with IL-MCAM Framework without TL: To validate the effectiveness of TL in the experiment, we conduct a comparison experiment between a model using TL and a model without TL during the re-training process, and the experimental results from three randomised experiments are shown in Fig. reffig:compare-freeze. The model without TL has 98.00%, 98.48%, and 98.21% of Spec., Sens. and F1, respectively, in the abnormal category. The Spec., Sens. and F1 of the model with TL in the abnormal category are 98.91%, 98.80% and 98.84%, respectively, which is an improvement of 0.91%, 0.32% and 0.63%, respectively, compared to the model without TL. The Spec., Sens. and F1 of the model without TL are 98.48%, 98.00%, and 98.25%, respectively, in the normal category. The Spec., Sens. and F1 of the model with TL in the normal category are 98.80%, 98.91% and 98.86%, respectively, which are 0.32%, 0.91% and 0.59% higher than those of the model without TL. The Avg.Acc. for the model without TL is 98.23%, whereas the Avg.Acc. of the model using TL is 98.85%, which is 0.62% higher than the model without TL. In summary, the comparison experiment illustrates that the proposed IL-MCAM framework using TL is better than the model without TL.

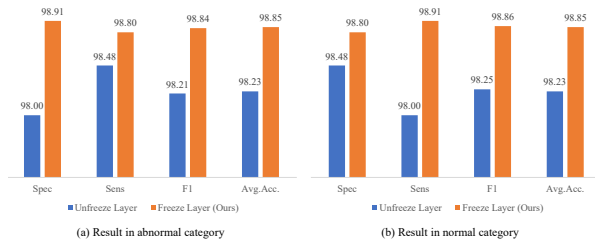


Figure 8: Performance analysis about whether to freeze the network layer in AL stage on test set. (a) is the performance in abnormal category. (b) is the performance in normal category. ([In %].)

Comparison with ensemble model without AM: To validate the effectiveness of the AM module in the experiment, we replaced SIC, MGIC and MSIC channels with traditional the VGG-16, Inception-V3 and Xception to obtain an ensemble model. The results of the ensemble model and IL-MCAM framework obtains from averages of three

randomised experiments, as shown in Fig. 9. The ensemble model has 98.29%, 99.02% and 98.64% of Spec., Sens. and F1 in the abnormal category. The IL-MCAM framework has 98.91%, 98.80% and 98.84% of Spec., Sens. and F1, respectively, in the abnormal category. Although Sens. is lower the IL-MCAM framework than the ensemble model, the most critical evaluation criterion, F1, is 0.20% higher. Similar results are obtained for the normal category. In addition, the Avg.Acc. of IL-MCAM framework is 98.85%, which is 0.20% higher than that of ensemble model. In summary, the IL-MCAM framework with added AM modules is more effective than the ensemble model composed of traditional deep learning models.

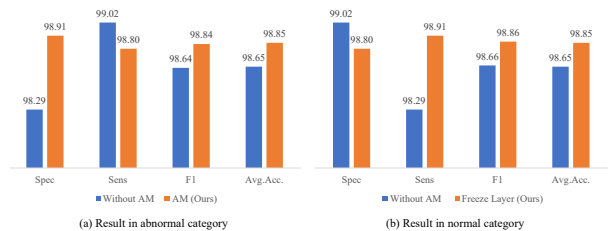


Figure 9: Performance analysis about whether to use AM in MCAM model on test set. (a) is the performance in abnormal category. (b) is the performance in normal category. ([In %].)

4.3. Extended Experiments

In this section, we describe the three conducted experiments. In Section 4.3.1, we describe the ablation experiments to verify the roles of the SIC, MGIC and MSIC modules in the IL-MCAM framework. In Section 4.3.2, we describe the experiment that used deep learning models combined with other AMs to implement the function of SIC, MGIC and MSIC to verify the interchangeability of the IL-MCAM framework. In Section 4.3.3, we describe the experiment that used the NCT-CRC-HE-100K dataset for multi-classification experiments to verify good generalisation ability of the IL-MCAM framework.

4.3.1. Ablation Experiment

To verify the role of the three channels in the IL-MCAM framework, we conduct ablation experiments according to the experimental setting described in Section 4.1.3. We list the results of the three randomised experiments in Table 6, and the importance of each channel as follows.

Table 5: Performance analysis of the proposed MCAM model and IL-MCAM approach along with the traditional models on test set. ([In %].)

Type	Model/Framework	Category	Spec.	Sens.	F1	Avg.Acc.
CNN	AlexNet [41]	Abnormal	93.50	96.35	94.90	94.90
		Normal	96.35	93.50	94.90	
	VGG-16 [42]	Abnormal	96.75	98.65	97.68	97.68
		Normal	98.65	96.75	97.69	
	Inception-V3 [45]	Abnormal	98.13	98.38	98.23	98.25
		Normal	98.38	98.13	98.26	
	ResNet-50 [43]	Abnormal	95.76	93.21	94.36	94.51
		Normal	93.21	95.76	94.65	
	Xception [46]	Abnormal	97.90	98.45	98.15	98.17
		Normal	98.45	97.90	98.19	
	ResNeXt-50 [48]	Abnormal	93.40	93.82	93.54	93.60
		Normal	93.82	93.40	93.68	
	InceptionResNet-V1 [47]	Abnormal	95.57	96.45	95.96	96.00
		Normal	96.45	95.57	96.04	
DenseNet-121 [44]	Abnormal	96.16	97.67	96.90	96.90	
	Normal	97.67	96.16	96.90		
VT	ViT [51]	Abnormal	77.90	74.90	75.80	76.42
		Normal	74.90	77.90	77.02	
	DeiT [52]	Abnormal	94.77	92.30	93.39	93.56
		Normal	92.30	94.77	93.72	
	BoTNet-50 [55]	Abnormal	94.48	95.54	94.96	95.01
		Normal	95.54	94.48	95.04	
	CaiT [53]	Abnormal	75.66	72.44	73.37	74.08
		Normal	72.44	75.66	74.74	
	CoaT [56]	Abnormal	73.89	87.94	81.89	80.82
		Normal	87.94	73.89	79.62	
	T2T-ViT [54]	Abnormal	90.15	92.00	91.03	91.05
		Normal	92.00	90.15	91.09	
	LeViT [57]	Abnormal	79.31	82.06	80.71	80.66
		Normal	82.06	79.31	80.62	
MLP	MLP-Mixer [58]	Abnormal	73.10	72.14	72.20	72.63
		Normal	72.14	73.10	73.00	
	gMLP [59]	Abnormal	88.07	88.96	88.42	88.51
		Normal	88.96	88.07	88.60	
ResMLP [60]	Abnormal	72.12	77.41	75.12	74.73	
	Normal	77.41	72.12	74.32		
Ours	MCAM	Abnormal	98.32	98.45	98.37	98.38
		Normal	98.45	98.32	98.41	
	IL-MCAM	Abnormal	98.91	98.80	98.84	98.85
		Normal	98.53	98.91	98.73	

Table 6: Results of the ablation experiments on the three channels obtained on test set. (\checkmark indicates that this channel is used. [In %].)

Channel		Category	1 st Experiment			2 nd Experiment			3 rd Experiment			Avg.acc.	
SIC	MGIC		MSIC	Sepe.	Sens.	F1	Sepe.	Sens.	F1	Sepe.	Sens.		F1
\checkmark			Abnormal	97.93	98.38	98.13	97.14	97.67	97.37	98.72	98.48	98.58	98.05 \pm 0.49
			Normal	98.38	97.93	98.17	97.67	97.14	97.43	98.48	98.72	98.62	
	\checkmark		Abnormal	98.72	99.09	98.89	98.22	98.68	98.43	99.09	98.72	98.89	98.75 \pm 0.21
			Normal	99.09	98.72	98.91	98.68	98.22	98.47	98.72	99.09	98.91	
		\checkmark	Abnormal	97.34	98.48	98.08	98.62	97.77	98.17	98.89	98.82	98.84	98.39 \pm 0.33
			Normal	98.48	97.34	98.12	97.77	98.62	98.23	98.82	98.89	98.87	
\checkmark	\checkmark		Abnormal	99.21	99.80	99.50	98.48	98.23	98.33	98.82	99.09	98.94	98.77 \pm 0.30
			Normal	99.80	99.21	99.50	98.23	98.48	98.37	99.09	98.82	98.96	
\checkmark		\checkmark	Abnormal	98.23	98.68	98.43	98.62	98.28	98.43	99.19	98.82	98.99	98.63 \pm 0.25
			Normal	98.68	98.23	98.46	98.28	98.62	98.48	98.82	99.19	99.01	
	\checkmark	\checkmark	Abnormal	99.41	99.80	99.60	98.62	98.28	98.43	99.09	98.82	98.93	98.77 \pm 0.22
			Normal	99.80	99.41	99.60	98.28	98.62	98.48	98.82	99.09	98.96	
\checkmark	\checkmark	\checkmark	Abnormal	99.41	99.80	99.60	98.62	98.38	98.48	99.49	98.82	99.14	98.85 \pm 0.26
			Normal	99.80	99.41	99.60	98.38	98.62	98.52	98.82	99.49	99.16	

First, through the ablation experiment in the second row, it can be observed that the Avg.Acc. using only MSIC is only 0.10% lower than that of IL-MCAM, and even in the second randomised experiment on the abnormal category Sens. is higher than the results obtained from the IL-MCAM framework. Meanwhile, it can be observed that the Avg.Acc. decreases more by 0.22% when the MSIC is removed from the ablation experiment in the fifth row. Importantly, these results indicate that the MSIC plays an irreplaceable role in the entire IL-MCAM framework.

Second, through the third row of ablation experiments, the Avg.Acc. using only MGIC is 0.46% lower than that of the IL-MCAM framework, and Sens. for the abnormal class in the third randomised experiment is equal to the results obtained from the IL-MCAM framework. Moreover, through the fourth row of the ablation experiment, the same Avg.Acc. is obtained with the MGIC removed as is obtained with the MSIC removed. Importantly, these results indicate that the MGIC plays a crucial role in the entire IL-MCAM framework.

Finally, it can be observed in the ablation experiment in the first row that the Avg.Acc. using only SIC is 0.80% lower than that of the IL-MCAM framework. Through the sixth row of the ablation experiment, there is a slight decrease of 0.08% in the Avg.Acc. after the SIC is removed. There is a slight decrease in the second and third randomised experiments and no decrease in the first randomised experiment, which indicates that the SIC plays role

in the overall IL-MCAM framework, but the effect is limited.

4.3.2. Interchangeability Experiment

To verify that the three modules in the IL-MCAM framework are interchangeable, we conduct the following an extended experiment using the experimental setting described in Section 4.1.3.

In SIC, CBAM [75] is used instead of SimAM [61] because CBAM [75] is similar to SimAM [61] in assigning weights to the spatial information of the VGG-16 model. In MGIC, ECA [65] and SRM [76] are similar to SE [63] and used to assign weights to the channel information to improve the ability of Inception-V3 model to extract multi-scale global information; therefore, ECA [65] and SRM [76] are used instead of SE [63]. In MSIC, SE [63] and SRM [76] are similar to ECA [65] and can assign weights to the channel information to improve the ability of Xception model to extract multi-scale global information; therefore, SE [63] and SRM [76] are used instead of ECA [65]. The results of the extended experiments to verify the interchangeability are listed in Table 7. The first to fourth rows are the replaced AM models, and the fifth row is the proposed IL-MCAM framework. We can observe that the classification accuracies of the four replaced models are 98.38% at the highest and 98.08% at the lowest level, which is a variation not more than 0.90% from the IL-MCAM framework and is a tolerable gap. Furthermore, in the second and third randomised experiments, the Spec. and Sens. of some replaced models in the abnormal category are

Table 7: Performance analysis of interchangeable experiments using different AMs in each of the three channels. ([In %].)

Channel			Category	1 st Experiment			2 nd Experiment			3 rd Experiment			Avg.Acc.
SIC	MGIC	MSIC		Sepec.	Sens.	F1	Sepec.	Sens.	F1	Sepec.	Sens.	F1	
CBAM	ECA	SRM	Abnormal	96.65	98.38	97.49	98.28	98.82	98.53	98.72	99.49	99.09	98.38 ± 0.66
			Normal	98.38	96.65	97.52	98.82	98.28	98.58	99.49	98.72	99.11	
CBAM	ECA	SE	Abnormal	96.94	98.89	97.89	98.81	98.38	98.58	98.72	99.29	98.99	98.50 ± 0.45
			Normal	98.89	96.94	97.91	98.38	98.81	98.62	99.29	98.72	97.52	
CBAM	SRM	SRM	Abnormal	97.04	98.28	97.64	98.92	98.08	98.47	97.93	99.39	98.64	98.27 ± 0.44
			Normal	98.28	97.04	97.67	98.08	98.92	98.53	99.39	97.93	98.66	
CBAM	SRM	SE	Abnormal	96.55	98.78	97.65	97.64	98.18	97.88	98.62	98.78	98.68	98.08 ± 0.44
			Normal	98.78	96.55	97.66	98.18	97.64	97.93	98.78	98.62	98.72	
SimAM	SE	ECA	Abnormal	98.62	99.19	98.89	98.62	98.38	98.48	99.49	98.82	99.14	98.85 ± 0.26
			Normal	99.19	98.62	98.91	98.38	98.62	98.52	98.82	99.49	99.16	

even higher than that of the IL-MCAM framework. In summary, the three channels of the IL-MCAM framework are interchangeable.

4.3.3. NCT-CRC-HE-100K Image Classification

To verify that the IL-MCAM framework has good generalisation ability, we carry out experiments on the publicly available CRC dataset NCT-CRC-HE-100K, composed of 100,000 patch-level images of nine different tissue categories, all of which are 224×224 pixels containing 0.5 microns per pixel. All images are colour-normalized using Macenko’s method [77, 78]. The nine different categories of tissue are adipose (ADI), background (BACK), debris (DEB), lymphocytes (LYM), mucus (MUC), smooth muscle (MUS), normal colon mucosa (NORM), cancer-associated stroma (STR) and colorectal adenocarcinoma epithelium (TUM), some of which are shown in Fig. 10. We divide the data in the ratio of 6:2:2 for the training, validation and test sets as shown in Table 8, and conduct extended experiments using the experimental parameters listed in Section 4.1.3.

The confusion matrix obtained using the MCAM model and the IL-MCAM framework on the test set of the NCT-CRC-100K dataset is shown in Fig. 11. When using the MCAM model for classification, 19933 images are correctly classified, 64 images are incorrectly classified, and 99.68% of Avg.Acc. is obtained. When using the IL-MCAM model for classification, 19952 images are correctly classified, 45 images are incorrectly classified, and 99.78% of Avg.Acc. is obtained. Compared with the classification results obtained by the MCAM model, IL-MCAM framework improves the classification accuracy in every category except for two fewer images correctly classified in the DEB category.

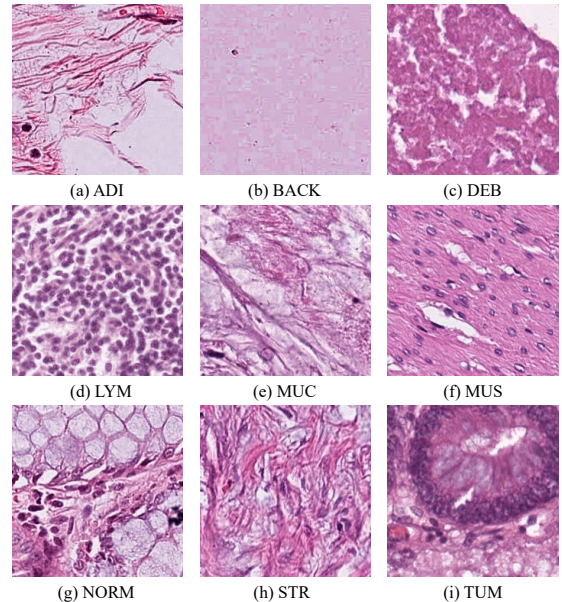


Figure 10: Some example of NCT-CRC-HE-100K.

Finally, we compare our method with previous experimental results obtained in NCT-CRC-HE-100K, and the comparison results are shown in Table 9. The best results in recent years are obtained by the method proposed by Ghosh et al. using the TL and ResNet methods, which obtained 99.76% Avg.Acc. Our proposed IL-MCAM framework obtained 99.78% Avg.Acc. which is 0.02% higher than the previous best result. This result indicates that the proposed IL-MCAM framework exhibits good classification performance and generalisation ability.

Predicted Class	ADI	2080 10.40%	0 0.00%	0 0.00%	0 0.00%	0 0.00%	1 0.01%	0 0.00%	0 0.00%	0 0.00%	99.95% 0.05%
	BACK	0 0.00%	2112 10.56%	0 0.00%	0 0.00%	0 0.00%	0 0.00%	0 0.00%	0 0.00%	0 0.00%	100.00% 0.00%
	DEB	0 0.00%	0 0.00%	2294 11.47%	0 0.00%	1 0.01%	1 0.01%	0 0.00%	1 0.01%	3 0.02%	99.74% 0.26%
	LYM	0 0.00%	0 0.00%	1 0.01%	2311 11.56%	0 0.00%	0 0.00%	1 0.01%	0 0.00%	0 0.00%	99.91% 0.09%
	MUC	0 0.00%	1 0.01%	0 0.00%	0 0.00%	1771 8.86%	0 0.00%	9 0.05%	0 0.00%	7 0.04%	99.04% 0.96%
	MUS	0 0.00%	0 0.00%	0 0.00%	0 0.00%	0 0.00%	2702 13.51%	1 0.01%	2 0.02%	0 0.00%	99.88% 0.12%
	NORM	0 0.00%	0 0.00%	0 0.00%	0 0.00%	1 0.01%	0 0.00%	1735 8.68%	0 0.00%	7 0.04%	99.54% 0.46%
	STR	1 0.01%	0 0.00%	4 0.02%	0 0.00%	1 0.01%	3 0.02%	0 0.00%	2085 10.43%	1 0.01%	99.43% 0.57%
	TUM	0 0.00%	0 0.00%	3 0.02%	0 0.00%	5 0.03%	0 0.00%	6 0.03%	1 0.01%	2843 14.22%	99.48% 0.52%
	Overall	99.95% 0.05%	99.95% 0.05%	99.65% 0.35%	100.00% 0.00%	99.55% 0.45%	99.82% 0.18%	99.03% 0.97%	99.81% 0.19%	99.30% 0.70%	99.68% 0.32%

(a) MCAM Model

Predicted Class	ADI	2081 10.41%	0 0.00%	0 0.00%	0 0.00%	0 0.00%	1 0.01%	0 0.00%	0 0.00%	0 0.00%	99.95% 0.05%
	BACK	0 0.00%	2112 10.56%	0 0.00%	0 0.00%	0 0.00%	0 0.00%	0 0.00%	0 0.00%	0 0.00%	100.00% 0.00%
	DEB	0 0.00%	0 0.00%	2292 11.46%	0 0.00%	1 0.01%	1 0.01%	0 0.00%	1 0.01%	3 0.02%	99.74% 0.26%
	LYM	0 0.00%	0 0.00%	1 0.01%	2311 11.56%	0 0.00%	0 0.00%	0 0.00%	0 0.00%	0 0.00%	99.96% 0.04%
	MUC	0 0.00%	1 0.01%	2 0.02%	0 0.00%	1777 8.89%	0 0.00%	0 0.00%	0 0.00%	7 0.04%	99.22% 0.78%
	MUS	0 0.00%	0 0.00%	0 0.00%	0 0.00%	0 0.00%	0 0.00%	2704 13.52%	4 0.02%	2 0.02%	99.93% 0.07%
	NORM	0 0.00%	0 0.00%	0 0.00%	0 0.00%	0 0.00%	0 0.00%	1744 8.72%	0 0.00%	6 0.03%	99.66% 0.34%
	STR	0 0.00%	0 0.00%	2 0.02%	0 0.00%	0 0.00%	1 0.01%	0 0.00%	2085 10.43%	1 0.01%	99.81% 0.19%
	TUM	0 0.00%	0 0.00%	5 0.03%	0 0.00%	2 0.02%	0 0.00%	3 0.02%	1 0.01%	2846 14.23%	99.62% 0.38%
	Overall	100.00% 0.00%	99.95% 0.05%	99.57% 0.43%	100.00% 0.00%	99.89% 0.11%	99.89% 0.11%	99.54% 0.46%	99.81% 0.19%	99.41% 0.59%	99.78% 0.22%

(b) IL-MCAM Framework

Figure 11: Confusion matrix obtained using MCAM model and IL-MCAM framework on test set of NCT-CRC-100K dataset.

Table 8: Data setting of HE-CRC-DS for training, validation and test sets.

Image Type	Training	Validation	Test
ADI	6245	2081	2081
BACK	6340	2113	2113
DEB	6908	2302	2302
LYM	6935	2311	2311
MUC	5338	1779	1779
MUS	8122	2707	2707
NORM	5258	1753	1752
STR	6268	2089	2089
TUM	8591	2863	2863
Sum	60005	19998	19997

4.4. Experimental Environment and Computational Time

In our experiments, the proposed IL-MCAM framework have an AL stage and an IL stage. In the AL stage, it took 1.23h to train the MCAM model in parallel. In IL stage, it took 5 min to label each misclassified image and 40 min to fine-tune the model. This experiment is carried out on a workstation. The running memory of the workstation is 32GB. It uses the Windows 10 Professional operating system and is equipped with an 8GB NVIDIA GeForce RTX 4000 GPU. Python 3.6, Pytorch 1.7.0, and Torchvision 0.9.0 are configured on the workstation.

Table 9: Comparison of the average accuracy of the proposed method with other methods in NCT-CRC-HE-100K. ([In %].)

References	Methods	Avg. Acc.
Kather et al. [79]	TL+VGG-16	98.70
Ghosh et al. [20]	Ensemble CNN	96.16
Hamida et al. [21]	TL+ResNet	99.76
Proposed	MCAM	99.68
Proposed	IL-MCAM	99.78

5. Discussion

This year, the rapid development of deep learning models has played a crucial role in the field of medical diagnosis. Classification of colorectal histopathological images plays a crucial role in the early prevention of diseases. In this paper, the proposed IL-MCAM framework is used for the classification of HE-CRC-DS and achieves good results.

Compared with regular images, medical images tend to be larger in size and the distribution of focused attention regions of the same class in medical images is not uniform in shape. Traditional CNN models using convolutional kernels tend to overconcentrate computational power on extracting edge information; therefore, we consider using a multi-channel approach combined with an attention mechanism to extract multi-scale information. VGG-16, Inception-V3 and Xception models

are generally considered to have a good ability to extract spatial information, multi-scale global information and multi-scale local information, and the combination of SimAM, SE and ECA attention mechanisms further improves the recognition accuracy. The IL-MCAM framework uses three channels, SIC, MSIC and MGIC, to enhance the width and ensure the complementarity of the extracted information. Meanwhile, three AMs are used to enhance the depth of the model to ensure the accuracy of the extracted information in each channel. The IL-MCAM framework enhances the classification performance in terms of width and depth. In summary, we select the models mentioned above to form the MCAM model.

Table 10 shows the model parameters and training time for comparing the proposed approaches with other traditional deep learning models. First, we can observe that the proposed MCAM model has very good results and has a significant improvement in classification results compared to traditional automatic methods using interactions. In addition, although the VT and MLP models are more effective than CNN models for routine tasks and have been shown to have a good ability to extract global information, these models do not work well in this experiment because of overfitting. The small medical training set leads to overfitting when trained on a complex or large model, and the experimental results validate this conclusion. In VT models, ViT and CaiT have large model parameters, but the experimental results are not satisfactory, and there are good classification results obtained by the lightweight DeiT and T2T-ViT. The same results are also obtained by the MLP models. Finally, owing to the complexity of the computational process caused by the complexity of the network, some small-scale models also require considerable com-

putation time. In contrast, three channels of SIC, MGIC and MSIC only use simple convolutional and AM blocks, and using parallel training techniques can significantly reduce computation the time of the three channels, so the IL-MCAM framework does not consume a lot of time for training although there are large model parameters.

Table 10: Model parameters and training time of comparing between the proposed approaches and other traditional deep learning models.

Model /Framework	Size (MB)	Time (s)
AlexNet [41]	217	1331
VGG-16 [42]	512	7060
Inception-V3 [45]	83.4	5340
ResNet-50 [43]	90	4772
Xception [46]	79.6	4015
ResNeXt-50 [48]	88	4564
InceptionResNet-V1 [47]	30.8	3260
DenseNet-121 [44]	27.1	2860
ViT [51]	31.2	1502
DeiT [52]	21.1	2566
BoTNet-50 [55]	72.1	4772
CaiT [53]	460	6956
CoaT [56]	20.6	3073
T2T-ViT [54]	15.5	2852
LeViT [57]	65.8	2943
MLP-Mixer [58]	225	11284
gMLP [59]	73.2	6396
ResMLP [60]	169	8943
MCAM	639	7060
IL-MCAM	639	7060

The confusion matrix for the three randomised experiments is shown in Fig. 7. To further analyse the causes of misclassification, we consulted the pathologists in detail and concluded the fol-

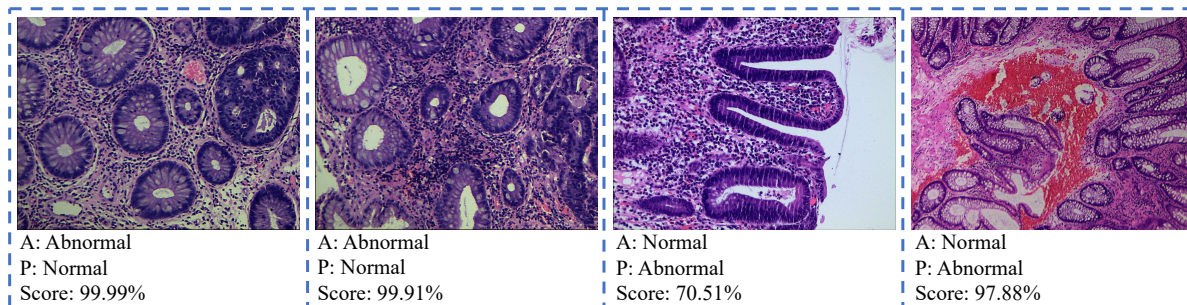


Figure 12: Examples of misclassified images from HE-CRC-DS.

lowing. Examples of misclassified images from the three randomised experiments are shown in Fig. 12. These examples can explain the three main reasons for the misclassification of HE-CRC-DS in the CHIC task using the proposed IL-MCAM framework. First, most of the lumen structure in Figs. 12-(a) and (b) is regular, and the cancer part occupies a small portion at the edge of the image, so the IL-MCAM framework classifies this image as normal during the testing phase. Second, Fig. 12-(c) is an image in the low grade category, where the nuclei of some of the luminal structures have started to enlarge, leading the IL-MCAM framework to classify the image as abnormal. Finally, Fig. 12-(d) shows an image from the normal category with blebs, which is misclassified owing to the presence of blebs.

6. Conclusion and Future Work

In this paper, we propose an IL-MCAM framework based on attention mechanisms and interactive learning for CHICs. The proposed IL-MCAM framework uses an MCAM model that combined different attention mechanisms for automatic learning. After automatic learning, the misclassified images are iteratively trained by manually labelling the attention regions to achieve the interactive process. Finally, evaluation metrics are obtained by testing. In the CHIC task, a significant performance improvement is observed in the proposed IL-MCAM approach compared with traditional deep learning models. In addition, we conduct three extended experiments: ablation experiments illustrate the role of each channel in the IL-MCAM framework; interchangeability experiments demonstrate the feasibility of designing three channels, and illustrate the interchangeability of the three channels, and extended experiments on the NCT-CRC-HE-100K dataset illustrate the generalisation ability of the IL-MCAM framework.

In the future, to accommodate different CHIC tasks, we plan to find the most suitable model for the current task from attention mechanisms and deep learning models using permutation and combination. We also plan to add attention mechanisms at different locations of deep learning models to analyse the impact of convolutional layers on classification performance in CHIC tasks.

Declaration of competing interest

The authors declare that they have no conflict of interest.

Acknowledgments

This work is supported by the “National Natural Science Foundation of China” (No.61806047) and the “Fundamental Research Funds for the Central Universities” (No. N2019003). We thank Miss Zixian Li and Mr. Guoxian Li for their important discussion.

References

- [1] M. Ganz, X. Yang, G. Slabaugh, Automatic segmentation of polyps in colonoscopic narrow-band imaging data, *IEEE Transactions on Biomedical Engineering* 59 (8) (2012) 2144–2151. doi:<https://doi.org/10.1109/TBME.2012.2195314>.
- [2] F. Bray, J. Ferlay, I. Soerjomataram, R. L. Siegel, L. A. Torre, A. Jemal, Global cancer statistics 2018: Globocan estimates of incidence and mortality worldwide for 36 cancers in 185 countries, *CA: a cancer journal for clinicians* 68 (6) (2018) 394–424. doi:<https://doi.org/10.3322/caac.21492>.
- [3] J. Zhou, R. Zheng, S. Zhang, H. Zeng, S. Wang, R. Chen, K. Sun, M. Li, J. Gu, G. Zhuang, et al., Colorectal cancer burden and trends: Comparison between china and major burden countries in the world, *Chinese Journal of Cancer Research* 33 (1) (2021) 1. doi:<https://doi.org/10.21147/j.issn.1000-9604.2021.01.01>.
- [4] M. A. Iftikhar, M. Hassan, H. Alquhayz, A colon cancer grade prediction model using texture and statistical features, smote and mrmr, in: 2016 19th International Multi-Topic Conference (INMIC), IEEE, 2016, pp. 1–7. doi:<https://doi.org/10.1109/INMIC.2016.7840161>.
- [5] F. Aeffner, K. Wilson, N. T. Martin, J. C. Black, C. L. L. Hendriks, B. Bolon, D. G. Rudmann, R. Gi-anani, S. R. Kogler, J. Krueger, et al., The gold standard paradox in digital image analysis: manual versus automated scoring as ground truth, *Archives of pathology & laboratory medicine* 141 (9) (2017) 1267–1275. doi:<https://doi.org/10.5858/arpa.2016-0386-RA>.
- [6] S. Ai, C. Li, X. Li, T. Jiang, M. Grzegorzec, C. Sun, M. M. Rahaman, J. Zhang, Y. Yao, H. Li, A state-of-the-art review for gastric histopathology image analysis approaches and future development, *BioMed Research International* 2021. doi:<https://doi.org/10.1155/2021/6671417>.
- [7] M. I. Jordan, T. M. Mitchell, Machine learning: Trends, perspectives, and prospects, *Science* 349 (6245) (2015) 255–260. doi:<https://doi.org/10.1126/science.aaa8415>.
- [8] Y. LeCun, Y. Bengio, G. Hinton, Deep learning, *nature* 521 (7553) (2015) 436–444. doi:<https://doi.org/10.1038/nature14539>.
- [9] L. Itti, C. Koch, E. Niebur, A model of saliency-based visual attention for rapid scene analysis, *IEEE Transactions on pattern analysis and machine intelligence*

- 20 (11) (1998) 1254–1259. doi:<https://doi.org/10.1109/34.730558>.
- [10] N. Linder, J. Konsti, R. Turkki, E. Rahtu, M. Lundin, S. Nordling, C. Haglund, T. Ahonen, M. Pietikäinen, J. Lundin, Identification of tumor epithelium and stroma in tissue microarrays using texture analysis, *Diagnostic pathology* 7 (1) (2012) 1–11. doi:<https://doi.org/10.1186/1746-1596-7-22>.
- [11] L. Jiao, Q. Chen, S. Li, Y. Xu, Colon cancer detection using whole slide histopathological images, in: *World Congress on Medical Physics and Biomedical Engineering* May 26-31, 2012, Beijing, China, Springer, 2013, pp. 1283–1286. doi:https://doi.org/10.1007/978-3-642-29305-4_336.
- [12] R. Peyret, A. Bouridane, S. A. Al-Maadeed, S. Kunhoth, F. Khelifi, Texture analysis for colorectal tumour biopsies using multispectral imagery, in: *2015 37th Annual International Conference of the IEEE Engineering in Medicine and Biology Society (EMBC)*, 2015, pp. 7218–7221. doi:<https://doi.org/10.1109/EMBC.2015.7320057>.
- [13] A. Chaddad, C. Desrosiers, A. Bouridane, M. Toews, L. Hassan, C. Tanougast, Multi texture analysis of colorectal cancer continuum using multispectral imagery, *PloS one* 11 (2) (2016) e0149893. doi:<https://doi.org/10.1371/journal.pone.0149893>.
- [14] J. N. Kather, C.-A. Weis, F. Bianconi, S. M. Melchers, L. R. Schad, T. Gaiser, A. Marx, F. G. Zöllner, Multi-class texture analysis in colorectal cancer histology, *Scientific reports* 6 (1) (2016) 1–11. doi:<https://doi.org/10.1038/srep27988>.
- [15] C. T. Sari, C. Gunduz-Demir, Unsupervised feature extraction via deep learning for histopathological classification of colon tissue images, *IEEE Transactions on Medical Imaging* 38 (5) (2019) 1139–1149. doi:<https://doi.org/10.1109/TMI.2018.2879369>.
- [16] J. Malik, S. Kiranyaz, S. Kunhoth, T. Ince, S. Al-Maadeed, R. Hamila, M. Gabbouj, Colorectal cancer diagnosis from histology images: A comparative study, *arXiv preprint arXiv:1903.11210*. URL <https://arxiv.org/abs/1903.11210>.
- [17] H. Yoon, J. Lee, J. E. Oh, H. R. Kim, S. Lee, H. J. Chang, D. K. Sohn, Tumor identification in colorectal histology images using a convolutional neural network, *Journal of digital imaging* 32 (1) (2019) 131–140. doi:<https://doi.org/10.1007/s10278-018-0112-9>.
- [18] N. Dif, Z. Elberrichi, A new deep learning model selection method for colorectal cancer classification, *International Journal of Swarm Intelligence Research (IJSIR)* 11 (3) (2020) 72–88. doi:<https://doi.org/10.4018/IJSIR.2020070105>.
- [19] H.-G. Nguyen, A. Blank, A. Lugli, I. Zlobec, An effective deep learning architecture combination for tissue microarray spots classification of h amp;e stained colorectal images, in: *2020 IEEE 17th International Symposium on Biomedical Imaging (ISBI)*, 2020, pp. 1271–1274. doi:<https://doi.org/10.1109/ISBI45749.2020.9098636>.
- [20] S. Ghosh, A. Bandyopadhyay, S. Sahay, R. Ghosh, I. Kundu, K. Santosh, Colorectal histology tumor detection using ensemble deep neural network, *Engineering Applications of Artificial Intelligence* 100 (2021) 104202. doi:<https://doi.org/10.1016/j.engappai.2021.104202>.
- [21] A. B. Hamida, M. Devanne, J. Weber, C. Truntzer, V. Derangère, F. Ghiringhelli, G. Forestier, C. Wemert, Deep learning for colon cancer histopathological images analysis, *Computers in Biology and Medicine* 136 (2021) 104730. doi:<https://doi.org/10.1016/j.combiomed.2021.104730>.
- [22] E. F. Ohata, J. V. S. das Chagas, G. M. Bezerra, M. M. Hassan, V. H. C. de Albuquerque, P. P. Reboucas Filho, A novel transfer learning approach for the classification of histological images of colorectal cancer, *The Journal of Supercomputing* (2021) 1–26doi:<https://doi.org/10.1007/s11227-020-03575-6>.
- [23] T. Sarkar, A. Hazra, N. Das, Classification of colorectal cancer histology images using image reconstruction and modified densenet, in: *International Conference on Computational Intelligence in Communications and Business Analytics*, Springer, 2021, pp. 259–271. URL https://link.springer.com/chapter/10.1007/978-3-030-75529-4_20
- [24] D. Sarwinda, R. H. Paradisa, A. Bustamam, P. Anggia, Deep learning in image classification using residual network (resnet) variants for detection of colorectal cancer, *Procedia Computer Science* 179 (2021) 423–431. doi:<https://doi.org/10.1016/j.procs.2021.01.025>.
- [25] M. M. Rahaman, C. Li, Y. Yao, F. Kulwa, M. A. Rahman, Q. Wang, S. Qi, F. Kong, X. Zhu, X. Zhao, Identification of covid-19 samples from chest x-ray images using deep learning: A comparison of transfer learning approaches, *Journal of X-ray Science and Technology* 28 (5) (2020) 821–839. doi:<https://doi.org/10.3233/XST-200715>.
- [26] C. Li, J. Zhang, F. Kulwa, S. Qi, Z. Qi, A sars-cov-2 microscopic image dataset with ground truth images and visual features, in: *Chinese Conference on Pattern Recognition and Computer Vision (PRCV)*, Springer, 2020, pp. 244–255. doi:https://doi.org/10.1007/978-3-030-60633-6_20.
- [27] S. Kosov, K. Shirahama, C. Li, M. Grzegorzec, Environmental microorganism classification using conditional random fields and deep convolutional neural networks, *Pattern recognition* 77 (2018) 248–261. doi:<https://doi.org/10.1016/j.patcog.2017.12.021>.
- [28] C. Li, K. Wang, N. Xu, A survey for the applications of content-based microscopic image analysis in microorganism classification domains, *Artificial Intelligence Review* 51 (4) (2019) 577–646. doi:<https://doi.org/10.1007/s10462-017-9572-4>.
- [29] J. Zhang, C. Li, S. Kosov, M. Grzegorzec, K. Shirahama, T. Jiang, C. Sun, Z. Li, H. Li, Lcunet: A novel low-cost u-net for environmental microorganism image segmentation, *Pattern Recognition* 115 (2021) 107885. doi:<https://doi.org/10.1016/j.patcog.2021.107885>.
- [30] X. Zhou, C. Li, M. M. Rahaman, Y. Yao, S. Ai, C. Sun, Q. Wang, Y. Zhang, M. Li, X. Li, et al., A comprehensive review for breast histopathology image analysis using classical and deep neural networks, *IEEE Access* 8 (2020) 90931–90956. doi:<https://doi.org/10.1109/ACCESS.2020.2993788>.
- [31] D. Xue, X. Zhou, C. Li, Y. Yao, M. M. Rahaman, J. Zhang, H. Chen, J. Zhang, S. Qi, H. Sun, An application of transfer learning and ensemble learning techniques for cervical histopathology image classification, *IEEE Access* 8 (2020) 104603–104618. doi:<https://doi.org/10.1109/ACCESS.2020.2999816>.
- [32] H. Chen, C. Li, X. Li, G. Wang, W. Hu, Y. Li,

- W. Liu, C. Sun, Y. Yao, Y. Teng, et al., Gashis-transformer: A multi-scale visual transformer approach for gastric histopathology image classification, arXiv preprint arXiv:2104.14528.
URL <https://arxiv.org/abs/2104.14528>
- [33] Y. Li, X. Wu, C. Li, X. Li, H. Chen, C. Sun, M. M. Rahaman, Y. Yao, Y. Zhang, T. Jiang, A hierarchical conditional random field-based attention mechanism approach for gastric histopathology image classification, *Applied Intelligence* (2022) 1–22doi:<https://doi.org/10.1007/s10489-021-02886-2>.
- [34] W. Hu, C. Li, X. Li, M. M. Rahaman, J. Ma, Y. Zhang, H. Chen, W. Liu, C. Sun, Y. Yao, et al., Gashissdb: A new gastric histopathology image dataset for computer aided diagnosis of gastric cancer, *Computers in biology and medicine* (2022) 105207doi:<https://doi.org/10.1016/j.combiomed.2021.105207>.
- [35] M. M. Rahaman, C. Li, X. Wu, Y. Yao, Z. Hu, T. Jiang, X. Li, S. Qi, A survey for cervical cytopathology image analysis using deep learning, *IEEE Access* 8 (2020) 61687–61710. doi:<https://doi.org/10.1109/ACCESS.2020.2983186>.
- [36] M. Mamunur Rahaman, C. Li, Y. Yao, F. Kulwa, X. Wu, X. Li, Q. Wang, Deepcervix: A deep learning-based framework for the classification of cervical cells using hybrid deep feature fusion techniques, *Computers in Biology and Medicine* 136 (2021) 104649.
URL <https://doi.org/10.1016/j.combiomed.2021.104649>
- [37] W. Liu, C. Li, M. M. Rahaman, T. Jiang, H. Sun, X. Wu, W. Hu, H. Chen, C. Sun, Y. Yao, et al., Is the aspect ratio of cells important in deep learning? a robust comparison of deep learning methods for multi-scale cytopathology cell image classification: From convolutional neural networks to visual transformers, *Computers in biology and medicine* (2021) 105026doi:<https://doi.org/10.1016/j.combiomed.2021.105026>.
- [38] X. Li, C. Li, F. Kulwa, M. M. Rahaman, W. Zhao, X. Wang, D. Xue, Y. Yao, Y. Cheng, J. Li, et al., Foldover features for dynamic object behaviour description in microscopic videos, *IEEE Access* 8 (2020) 114519–114540. doi:<https://doi.org/10.1109/ACCESS.2020.3003993>.
- [39] A. Chen, C. Li, S. Zou, M. M. Rahaman, Y. Yao, H. Chen, H. Yang, P. Zhao, W. Hu, W. Liu, et al., Svia dataset: A new dataset of microscopic videos and images for computer-aided sperm analysis, *Biocybernetics and Biomedical Engineering*doi:<https://doi.org/10.1016/j.bbe.2021.12.010>.
- [40] Y. LeCun, B. Boser, J. S. Denker, D. Henderson, R. E. Howard, W. Hubbard, L. D. Jackel, Backpropagation applied to handwritten zip code recognition, *Neural Computation* 1 (4) (1989) 541–551. doi:<https://doi.org/10.1162/neco.1989.1.4.541>.
- [41] A. Krizhevsky, I. Sutskever, G. E. Hinton, Imagenet classification with deep convolutional neural networks, *Advances in neural information processing systems* 25 (2012) 1097–1105. doi:<https://doi.org/10.1145/3065386>.
- [42] K. Simonyan, A. Zisserman, Very deep convolutional networks for large-scale image recognition, arXiv preprint arXiv:1409.1556.
URL <https://arxiv.org/abs/1409.1556>
- [43] K. He, X. Zhang, S. Ren, J. Sun, Deep residual learning for image recognition, in: *Proceedings of the IEEE conference on computer vision and pattern recognition*, 2016, pp. 770–778. doi:<https://doi.org/10.1109/CVPR.2016.90>.
- [44] G. Huang, Z. Liu, L. Van Der Maaten, K. Q. Weinberger, Densely connected convolutional networks, in: *Proceedings of the IEEE conference on computer vision and pattern recognition*, 2017, pp. 4700–4708. doi:<https://doi.org/10.1109/CVPR.2017.243>.
- [45] C. Szegedy, V. Vanhoucke, S. Ioffe, J. Shlens, Z. Wojna, Rethinking the inception architecture for computer vision, in: *Proceedings of the IEEE conference on computer vision and pattern recognition*, 2016, pp. 2818–2826. doi:<https://doi.org/10.1109/CVPR.2016.308>.
- [46] F. Chollet, Xception: Deep learning with depthwise separable convolutions, in: *2017 IEEE Conference on Computer Vision and Pattern Recognition (CVPR)*, 2017, pp. 1800–1807. doi:<https://doi.org/10.1109/CVPR.2017.195>.
- [47] C. Szegedy, S. Ioffe, V. Vanhoucke, A. A. Alemi, Inception-v4, inception-resnet and the impact of residual connections on learning, in: *Thirty-first AAAI conference on artificial intelligence*, 2017, pp. 4278–4284. doi:<https://dl.acm.org/doi/10.5555/3298023.3298188>.
- [48] S. Xie, R. Girshick, P. Dollár, Z. Tu, K. He, Aggregated residual transformations for deep neural networks, in: *Proceedings of the IEEE conference on computer vision and pattern recognition*, 2017, pp. 1492–1500. doi:<https://doi.org/10.1109/CVPR.2017.634>.
- [49] A. Vaswani, N. Shazeer, N. Parmar, J. Uszkoreit, L. Jones, A. N. Gomez, L. Kaiser, I. Polosukhin, Attention is all you need, in: *Advances in neural information processing systems*, 2017, pp. 5998–6008.
URL <https://arxiv.org/abs/1706.03762>
- [50] S. Khan, M. Naseer, M. Hayat, S. W. Zamir, F. S. Khan, M. Shah, Transformers in vision: A survey, arXiv preprint arXiv:2101.01169.
URL <https://arxiv.org/abs/2101.01169>
- [51] A. Dosovitskiy, L. Beyer, A. Kolesnikov, D. Weissenborn, X. Zhai, T. Unterthiner, M. Dehghani, M. Minderer, G. Heigold, S. Gelly, et al., An image is worth 16x16 words: Transformers for image recognition at scale, arXiv preprint arXiv:2010.11929.
URL <https://arxiv.org/abs/2010.11929>
- [52] H. Touvron, M. Cord, M. Douze, F. Massa, A. Sablayrolles, H. Jégou, Training data-efficient image transformers & distillation through attention, in: *International Conference on Machine Learning*, PMLR, 2021, pp. 10347–10357.
URL <https://proceedings.mlr.press/v139/touvron21a.html>
- [53] H. Touvron, M. Cord, A. Sablayrolles, G. Synnaeve, H. Jégou, Going deeper with image transformers, arXiv preprint arXiv:2103.17239.
URL <https://arxiv.org/abs/2103.17239>
- [54] L. Yuan, Y. Chen, T. Wang, W. Yu, Y. Shi, Z. Jiang, F. E. Tay, J. Feng, S. Yan, Tokens-to-token vit: Training vision transformers from scratch on imagenet, arXiv preprint arXiv:2101.11986.
URL <https://arxiv.org/abs/2101.11986>
- [55] A. Srinivas, T.-Y. Lin, N. Parmar, J. Shlens, P. Abbeel, A. Vaswani, Bottleneck transformers for visual recognition, in: *2021 IEEE/CVF Conference on Computer Vision and Pattern Recognition (CVPR)*, 2021, pp. 16514–16524. doi:<https://doi.org/10.1109/>

- CVPR46437.2021.01625.
- [56] W. Xu, Y. Xu, T. Chang, Z. Tu, Co-scale conv-attentional image transformers, arXiv preprint arXiv:2104.06399.
URL <https://arxiv.org/abs/2104.06399>
- [57] B. Graham, A. El-Nouby, H. Touvron, P. Stock, A. Joulin, H. Jégou, M. Douze, Levit: a vision transformer in convnet’s clothing for faster inference, arXiv preprint arXiv:2104.01136.
URL <https://arxiv.org/abs/2104.01136>
- [58] I. Tolstikhin, N. Houlsby, A. Kolesnikov, L. Beyer, X. Zhai, T. Unterthiner, J. Yung, A. P. Steiner, D. Keysers, J. Uszkoreit, et al., Mlp-mixer: An all-mlp architecture for vision, in: Thirty-Fifth Conference on Neural Information Processing Systems, 2021, pp. 1–12.
URL <https://arxiv.org/abs/2105.01601>
- [59] H. Liu, Z. Dai, D. R. So, Q. V. Le, Pay attention to mlps, arXiv preprint arXiv:2105.08050.
URL <https://arxiv.org/abs/2105.08050>
- [60] H. Touvron, P. Bojanowski, M. Caron, M. Cord, A. El-Nouby, E. Grave, A. Joulin, G. Synnaeve, J. Verbeek, H. Jégou, Resmlp: Feedforward networks for image classification with data-efficient training, arXiv preprint arXiv:2105.03404.
URL <https://arxiv.org/abs/2105.03404>
- [61] L. Yang, R. Zhang, L. Li, X. Xie, Simam: A simple, parameter-free attention module for convolutional neural networks, in: International Conference on Machine Learning, PMLR, 2021, pp. 11863–11874.
URL <https://proceedings.mlr.press/v139/yang21o.html>
- [62] C. Szegedy, V. Vanhoucke, S. Ioffe, J. Shlens, Z. Wojna, Rethinking the inception architecture for computer vision, in: 2016 IEEE Conference on Computer Vision and Pattern Recognition (CVPR), 2016, pp. 2818–2826. doi:<https://doi.org/10.1109/CVPR.2016.308>.
- [63] J. Hu, L. Shen, S. Albanie, G. Sun, E. Wu, Squeeze-and-excitation networks, IEEE Transactions on Pattern Analysis and Machine Intelligence 42 (8) (2020) 2011–2023. doi:<https://doi.org/10.1109/TPAMI.2019.2913372>.
- [64] F. Chollet, Xception: Deep learning with depthwise separable convolutions, in: 2017 IEEE Conference on Computer Vision and Pattern Recognition (CVPR), 2017, pp. 1800–1807. doi:<https://doi.org/10.1109/CVPR.2017.195>.
- [65] Q. Wang, B. Wu, P. Zhu, P. Li, W. Zuo, Q. Hu, Eca-net: Efficient channel attention for deep convolutional neural networks, in: 2020 IEEE/CVF Conference on Computer Vision and Pattern Recognition (CVPR), 2020, pp. 11531–11539. doi:<https://doi.org/10.1109/CVPR42600.2020.01155>.
- [66] W. Rawat, Z. Wang, Deep convolutional neural networks for image classification: A comprehensive review, Neural computation 29 (9) (2017) 2352–2449. doi:https://doi.org/10.1162/neco_a_00990.
- [67] C. Szegedy, W. Liu, Y. Jia, P. Sermanet, S. Reed, D. Anguelov, D. Erhan, V. Vanhoucke, A. Rabinovich, Going deeper with convolutions, in: Proceedings of the IEEE conference on computer vision and pattern recognition, 2015, pp. 1–9. doi:<https://doi.org/10.1109/CVPR.2015.7298594>.
- [68] L. Sifre, S. Mallat, Rigid-motion scattering for texture classification, arXiv preprint arXiv:1403.1687doi:<https://arxiv.org/abs/1403.1687>.
- [69] M. Raghu, C. Zhang, J. Kleinberg, S. Bengio, Transfusion: Understanding transfer learning for medical imaging, arXiv preprint arXiv:1902.07208doi:<https://arxiv.org/abs/1902.07208>.
- [70] S. J. Pan, Q. Yang, A survey on transfer learning, IEEE Transactions on knowledge and data engineering 22 (10) (2009) 1345–1359. doi:<https://doi.org/10.1109/TKDE.2009.191>.
- [71] Z. Niu, G. Zhong, H. Yu, A review on the attention mechanism of deep learning, Neurocomputing 452 (2021) 48–62. doi:<https://doi.org/10.1016/j.neucom.2021.03.091>.
- [72] B. S. Webb, N. T. Dhruv, S. G. Solomon, C. Tailby, P. Lennie, Early and late mechanisms of surround suppression in striate cortex of macaque, Journal of Neuroscience 25 (50) (2005) 11666–11675. doi:<https://doi.org/10.1523/JNEUROSCI.3414-05.2005>.
- [73] F. M. Castro, M. J. Marín-Jiménez, N. Guil, C. Schmid, K. Alahari, End-to-end incremental learning, in: Proceedings of the European conference on computer vision (ECCV), 2018, pp. 233–248. doi:https://doi.org/10.1007/978-3-030-01258-8_15.
- [74] I. Loshchilov, F. Hutter, Fixing weight decay regularization in adam (2018).
URL <https://openreview.net/forum?id=rk6qdGgCZ>
- [75] S. Woo, J. Park, J.-Y. Lee, I. S. Kweon, Cbam: Convolutional block attention module, in: Proceedings of the European conference on computer vision (ECCV), 2018, pp. 3–19. doi:https://doi.org/10.1007/978-3-030-01234-2_1.
- [76] H. Lee, H.-E. Kim, H. Nam, Srm: A style-based recalibration module for convolutional neural networks, in: Proceedings of the IEEE/CVF International Conference on Computer Vision, 2019, pp. 1854–1862. doi:<https://doi.org/10.1109/ICCV.2019.00194>.
- [77] M. Macenko, M. Niethammer, J. S. Marron, D. Borland, J. T. Woosley, X. Guan, C. Schmitt, N. E. Thomas, A method for normalizing histology slides for quantitative analysis, in: 2009 IEEE International Symposium on Biomedical Imaging: From Nano to Macro, IEEE, 2009, pp. 1107–1110. doi:<https://doi.org/10.1109/ISBI.2009.5193250>.
- [78] J. N. Kather, N. Halama, A. Marx, 100,000 histological images of human colorectal cancer and healthy tissue (Apr. 2018). doi:<https://doi.org/10.5281/zenodo.1214456>.
- [79] J. N. Kather, J. Krisam, P. Charoentong, T. Luedde, E. Herpel, C.-A. Weis, T. Gaiser, A. Marx, N. A. Valous, D. Ferber, et al., Predicting survival from colorectal cancer histology slides using deep learning: A retrospective multicenter study, PLoS medicine 16 (1) (2019) e1002730. doi:<https://doi.org/10.1371/journal.pmed.1002730>.